

## Myeloid cell interferon secretion restricts Zika flavivirus infection of developing and malignant human neural progenitor cells

### Highlights

- Glioblastoma is refractory to Zika virus (ZIKV) compared with human developing brain
- Myeloid cell interferon secretion restricts ZIKV infection in glioblastoma (GBM)
- Clinical inhibitors of JAK/STAT signaling enhance ZIKV infection in GBM cells
- Myeloid cell coculture or interferon protects the developing brain from ZIKV infection

### Authors

Harry Bulstrode, Gemma C. Girdler,  
Tannia Gracia, ..., Omer Bayraktar,  
Fanni Gergely, David H. Rowitch

### Correspondence

hb252@cam.ac.uk (H.B.),  
fanni.gergely@bioch.ox.ac.uk (F.G.),  
dhr25@medsch.cam.ac.uk (D.H.R.)

### In brief

Zika virus (ZIKV) infects parallel neural progenitor cell populations in the developing brain and in glioblastoma brain tumors. Bulstrode et al. demonstrate that interferon secretion by human brain myeloid cells can render each neural progenitor population refractory to ZIKV infection, with important implications for neuroprotection and viral oncolysis.



## Article

# Myeloid cell interferon secretion restricts Zika flavivirus infection of developing and malignant human neural progenitor cells

Harry Bulstrode,<sup>1,2,14,\*</sup> Gemma C. Girdler,<sup>1,2,14</sup> Tannia Gracia,<sup>3,14</sup> Alexander Aivazidis,<sup>4</sup> Ilias Moutsopoulos,<sup>1</sup> Adam M.H. Young,<sup>1,2</sup> John Hancock,<sup>3</sup> Xiaoling He,<sup>1</sup> Katherine Ridley,<sup>1,5</sup> Zhaoyang Xu,<sup>1,5</sup> John H. Stockley,<sup>1,5</sup> John Finlay,<sup>1,5</sup> Clement Hallou,<sup>1,5</sup> Teodoro Fajardo,<sup>6,7</sup> Daniel M. Fountain,<sup>8</sup> Stijn van Dongen,<sup>4</sup> Alexis Joannides,<sup>2</sup> Robert Morris,<sup>2</sup> Richard Mair,<sup>2</sup> Colin Watts,<sup>9</sup> Thomas Santarius,<sup>2</sup> Stephen J. Price,<sup>2</sup> Peter J.A. Hutchinson,<sup>2</sup> Emma J. Hodson,<sup>10</sup> Steven M. Pollard,<sup>11</sup> Irina Mohorianu,<sup>1</sup> Roger A. Barker,<sup>1</sup> Trevor R. Sweeney,<sup>6,12</sup> Omer Bayraktar,<sup>4</sup> Fanni Gergely,<sup>3,13,\*</sup> and David H. Rowitch<sup>1,4,5,15,\*</sup>

<sup>1</sup>Wellcome MRC Cambridge Stem Cell Institute, University of Cambridge, Cambridge CB2 0AW, UK

<sup>2</sup>Division of Academic Neurosurgery, Department of Clinical Neurosciences, University of Cambridge, Cambridge CB2 0QQ, UK

<sup>3</sup>Cancer Research UK Cambridge Institute, University of Cambridge, Cambridge CB2 0RE, UK

<sup>4</sup>Wellcome Sanger Institute, Hinxton CB10 1SA, UK

<sup>5</sup>Department of Paediatrics, University of Cambridge, Cambridge CB2 0QQ, UK

<sup>6</sup>Department of Virology, University of Cambridge, Cambridge CB2 0QQ, UK

<sup>7</sup>Department of Virology, Royal London Hospital, Barts Health NHS Trust, London E1 2ES, UK

<sup>8</sup>Manchester Centre for Clinical Neurosciences, Manchester M6 8HD, UK

<sup>9</sup>Institute of Cancer and Genomic Sciences, University of Birmingham, Birmingham B15 2SY, UK

<sup>10</sup>Experimental Medicine and Immunotherapeutics, University of Cambridge, Cambridge CB2 0QQ, UK

<sup>11</sup>Centre for Regenerative Medicine and Cancer Research UK Edinburgh Centre, Institute for Regeneration and Repair, University of Edinburgh, Edinburgh EH16 4UU, UK

<sup>12</sup>The Pirbright Institute, Guildford, Surrey GU24 0NF, UK

<sup>13</sup>Department of Biochemistry, University of Oxford, Oxford OX1 3QU, UK

<sup>14</sup>These authors contributed equally

<sup>15</sup>Lead contact

\*Correspondence: hb252@cam.ac.uk (H.B.), fanni.gergely@bioch.ox.ac.uk (F.G.), dhr25@medsch.cam.ac.uk (D.H.R.)

<https://doi.org/10.1016/j.neuron.2022.09.002>

## SUMMARY

Zika virus (ZIKV) can infect human developing brain (HDB) progenitors resulting in epidemic microcephaly, whereas analogous cellular tropism offers treatment potential for the adult brain cancer, glioblastoma (GBM). We compared productive ZIKV infection in HDB and GBM primary tissue explants that both contain SOX2+ neural progenitors. Strikingly, although the HDB proved uniformly vulnerable to ZIKV infection, GBM was more refractory, and this correlated with an innate immune expression signature. Indeed, GBM-derived CD11b+ microglia/macrophages were necessary and sufficient to protect progenitors against ZIKV infection in a non-cell autonomous manner. Using SOX2+ GBM cell lines, we found that CD11b+-conditioned medium containing type 1 interferon beta (IFN $\beta$ ) promoted progenitor resistance to ZIKV, whereas inhibition of JAK1/2 signaling restored productive infection. Additionally, CD11b+ conditioned medium, and IFN $\beta$  treatment rendered HDB progenitor lines and explants refractory to ZIKV. These findings provide insight into neuroprotection for HDB progenitors as well as enhanced GBM oncolytic therapies.

## INTRODUCTION

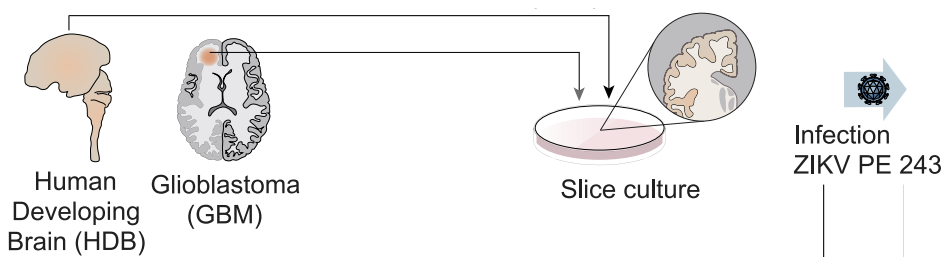
Viral infections of human brain during early development can result in congenital pathology, death, and lifelong disability (Me-gli and Coyne, 2021). A recently recognized congenital (aka, “TORCH”) infection is caused by Zika virus (ZIKV), a mosquito-borne positive strand RNA flavivirus (for list of abbreviations see Table S1). An estimated 5%–10% of babies born to mothers infected during pregnancy with ZIKV epidemic strains exhibit

features of Zika congenital syndrome including microcephaly and/or neurodevelopmental delay (Cugola et al., 2016), whereas few sequelae of ZIKV infection have been reported in the adult brain (Carod-Artal, 2018).

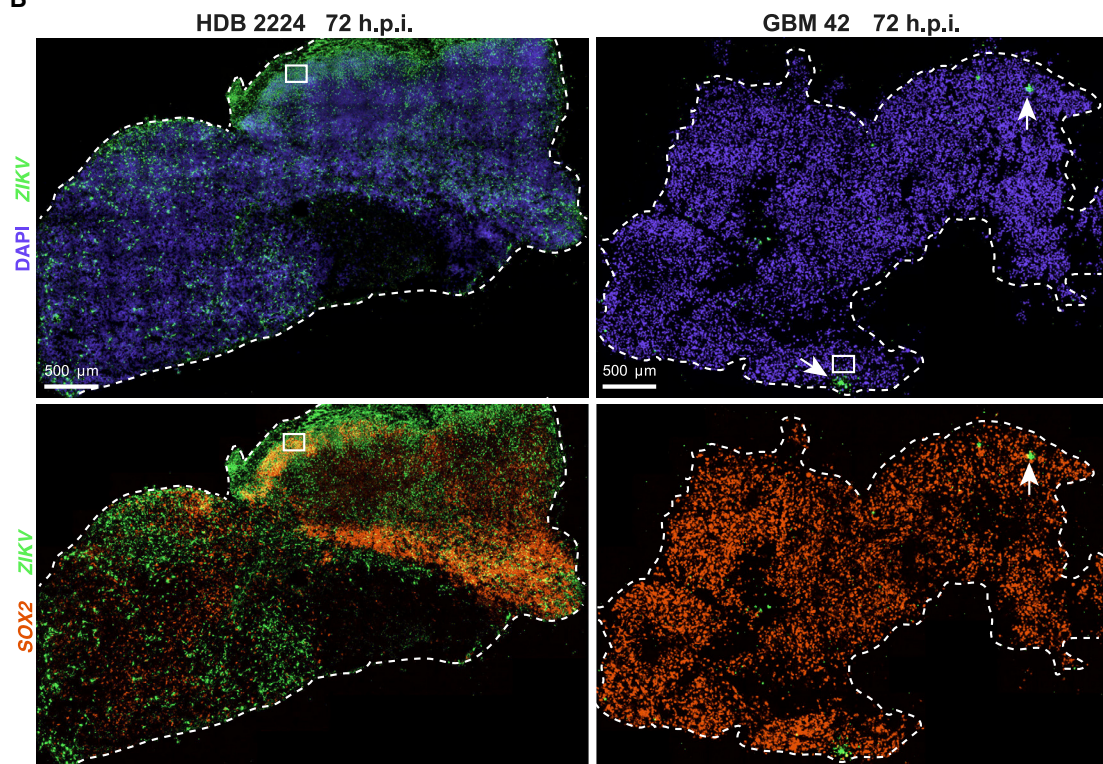
ZIKV epidemic strains including PE243 (ZIKV-PE243), identified in Brazil in 2015 and the basis for our studies (Donald et al., 2016), have been shown to infect human neural progenitor cells marked by expression of SOX2 (Chavali et al., 2017; Li et al., 2016; Retallack et al., 2016), an SRY-box transcription factor



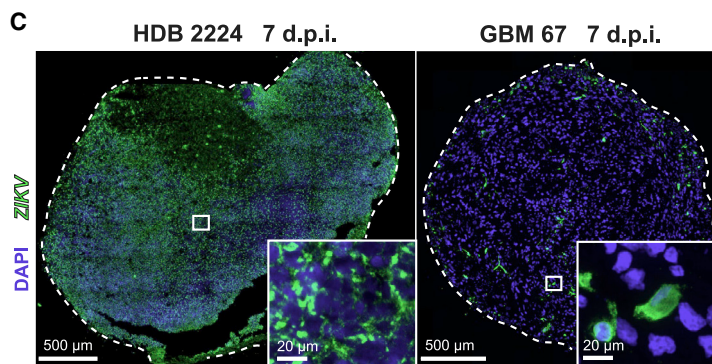
**A**



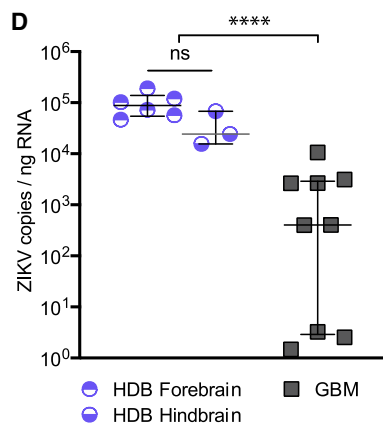
**B**



**C**



**D**



(legend on next page)

(Wegner and Stolt, 2005). Alongside their developmental role, SOX2 and related neural lineage transcription factors drive proliferation and invasion of cancer stem cells in malignant primary brain tumors including glioblastoma (GBM) (Bulstrode et al., 2017; Sturm et al., 2014; Suvà et al., 2014). Glioma stem cells are resistant to host immune attack and to current treatment (Bao et al., 2006; Gangoso et al., 2021; Mehta et al., 2011), suggesting them as a prime target for novel GBM therapy (Gimple et al., 2019; Suvà and Tirosh, 2020; Wang et al., 2020). In this regard, repurposing pathogenic viruses offers treatment promise, directly through cancer stem cell lysis and indirectly through immune stimulation (Harrington et al., 2019). ZIKV has demonstrated oncolytic potential in GBM, prolonging survival in a mouse GBM model (Zhu et al., 2017). However, virus-based strategies have yet to demonstrate consistent clinical benefit in brain cancer (Zhang and Liu, 2020), in part reflecting limitations in the available cell and animal models, especially in capturing the human tissue microenvironment (Liu et al., 2013).

SOX2 expression has been reported to mark diverse ZIKV target cells including neural progenitor cells, oligodendrocyte precursor cells, astrocytes (Garcez et al., 2016; Retallack et al., 2016; Souza et al., 2016), and glioma stem cells (Chen et al., 2018; Zhu et al., 2017, 2020). Nevertheless, human embryonic stem cells and iPSCs are not highly permissive to ZIKV infection, despite high SOX2 expression and proliferative capacity (Tang et al., 2016), suggesting that additional factors are involved. Here, we investigated productive ZIKV infection in progenitor cell populations in primary HDB versus GBM. We found striking differences in relative rates of infection between these explants that could not simply be accounted for by cell-intrinsic factors such as SOX2 expression levels. We go on to show that non-cell-autonomous microenvironmental factors secreted from myeloid cells are both necessary and sufficient to regulate productive infection of HDB and GBM progenitor cells.

## RESULTS

### SOX2+ progenitor cells in human developing brain are vulnerable to ZIKV infection, whereas GBM progenitors are refractory

We first compared rates of ZIKV-PE243 productive infection in explant slice cultures from HDB (9–12 weeks gestational age, n = 2 specimens, including forebrain and hindbrain regions from both specimens) and human adult GBM (n = 3 patient samples). As shown (Figures 1A, 1B, and S1A–S1D), whereas HDB samples were permissive to infection, GBM slices were refractory to ZIKV, as measured by single molecule fluorescent *in situ* hybridization (smFISH) and immunofluorescence (IF) at 72 h post infection (hpi) (for list of abbreviations see Table S1). We noted that infection tended to be patchy and restricted to cells at the tissue surface at

48–72 hpi in both HDB (Figure S1A) and GBM. In view of the longer time needed for ZIKV to penetrate thick tissues slices in culture and to be consistent with prior study endpoints (Zhu et al., 2017; Muffat et al., 2018), we also scored 7 days post infection (7 dpi; Figures 1C, 1D, S1A, S1E, and S1F). Quantitative polymerase chain reaction (real-time [RT]-qPCR) assay of viral genome copy number confirmed a significant difference in productive virus levels between HDB and GBM samples at 7 dpi (Figure 1D), at which point, HDB explant tissue showed more extensive ZIKV infection and apoptosis compared with GBM tissue that was relatively intact (Figures S1E and S1F).

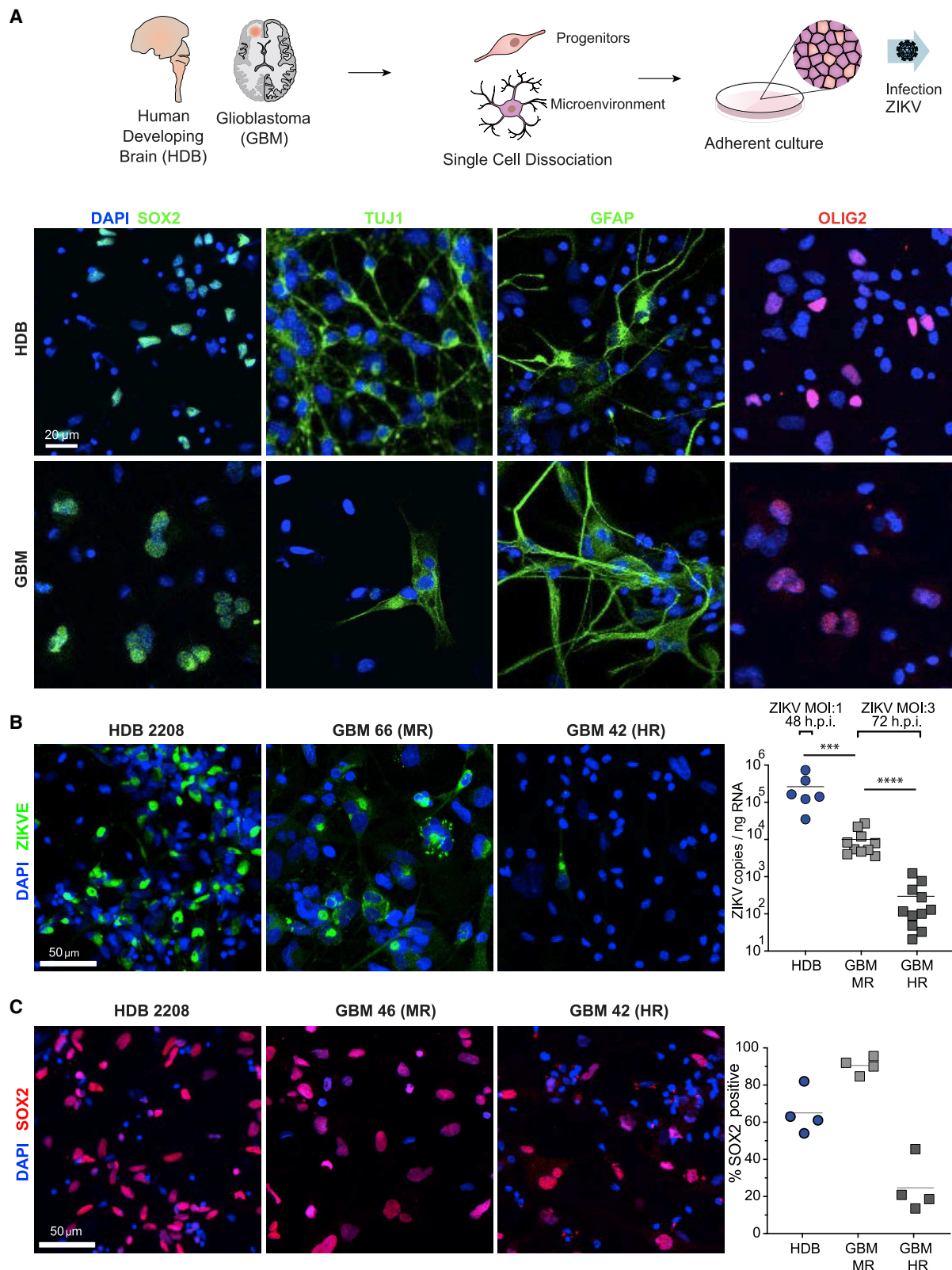
To assess the potential of cell-intrinsic contributions to differential ZIKV vulnerability in progenitor cells, we quantified virus levels by RT-qPCR 48 hpi-adherent serum-free cultures of HDB cell lines derived from forebrain and hindbrain at 10 (HDB FB1 and HB1) or 12 weeks (HDB FB12 and HB12) gestation, as well as cell lines from pediatric diffuse H3K27M pontine midline glioma (DMG 007, DMG B117, and DMG B169) and cell lines derived from adult GBM (GBM E22, GBM E25, and GBM E34). In keeping with previous reports using cell lines (Zhu et al., 2017, 2020), productive viral infection and consequent lytic cell death ensued in GBM as well as in HDB cell lines over 48–96 h (Figures S2A and S2B). The cell lines began to detach at 48–72 hpi compromising the accuracy of RT-qPCR assays beyond these time points. The finding that GBM progenitor lines were vulnerable to ZIKV—in contrast to findings with refractory primary GBM slice explants—initially suggested a role for non-cell autonomous regulation by microenvironmental factors.

We next dissociated primary HDB and GBM tissue to single-cell suspension, generating adherent primary cultures comprising diverse cell identities (Figures 2A and S2C–S2E). We observed that all six HDB cultures tested (8–9 weeks gestational age, including one sample pair from forebrain and hindbrain of a single specimen) showed productive ZIKV infection by RT-qPCR (Figure 2B). We performed similar ZIKV infection on 20 primary dissociated GBM cultures and found that productive viral infection was 10- to 100-fold lower than HDB. This necessitated 3-fold higher multiplicity of infection (MOI 3) in GBM versus HDB (MOI 1) and longer exposure in GBM (72 h) versus HDB (48 h) for GBM to achieve detectable levels of productive infection. Indeed, relative to HDB, all GBM cultures were refractory to ZIKV infection. Moreover, we could clearly divide GBMs into moderately refractory (MR) or highly refractory (HR) to infection based on viral RNA levels by RT-qPCR (Figure 2B).

Consistent with prior findings of SOX2 being a key determinant of ZIKV infection (Zhu et al., 2020), the proportion of cells positive for SOX2 was higher in MR than HR GBM samples (Figures 2C and S2E), whereas there was no significant difference in the fraction of cells labeled by the proliferation marker MKI67 (Figure S2F). Interestingly, despite higher productive infection in

**Figure 1. Human developing brain organotypic slices are vulnerable to ZIKV, whereas GBM slices are refractory**

- (A) Primary HDB and GBM samples were processed for slice culture, then infected with ZIKV PE243.
- (B) RNAscope smFISH of representative ZIKV-infected HDB and GBM slice cultures with ZIKV  $1 \times 10^7$  PFU, 72 h post infection (hpi), using SOX2 (red) and ZIKV (green) probes. White arrow denotes ZIKV infection.
- (C) smFISH of ZIKV-infected HDB and GBM slice cultures with ZIKV  $1 \times 10^7$  PFU, 7 days post infection (dpi), using ZIKV probe (green).
- (D) RT-qPCR of ZIKV in HDB and GBM slice cultures, infected with ZIKV  $1 \times 10^7$  PFU, 7 dpi, (median and interquartile range indicated. \*\*\* Mann-Whitney U test p < 0.0001). Data points represent replicate slices from HDB n = 2 specimens, both with hindbrain (hb) and forebrain (fb) regions, and GBM n = 3 patients.



(legend on next page)

HDB samples, the proportion of SOX2+ cells was higher in MR GBM than that in HDB (Figure 2C), indicating that the SOX2+ composition alone could not account for differential vulnerability in HDB versus GBM. Together, these findings suggested that non-cell autonomous (e.g., microenvironment) factors regulated ZIKV progenitor cell infection.

### ZIKV-refractory GBM displays an innate immune signature

We next infected freshly dissociated primary HDB and GBM cultures with a ZIKV-mCherry (ZIKV-mCh) live transgenic reporter virus (Mutso et al., 2017), then performed fluorescence activated cell sorting (FACS) and bulk RNA sequencing (RNA-seq) of both ZIKV-mCh-positive (ZIKV-mCh+) and -negative fractions (Figures 3A, 3B, and S3A). As expected, MR GBMs yielded higher ZIKV-mCh+ fractions than HR GBMs (Figure S3B).

We next used expression data to ask whether cell-intrinsic factors beyond SOX2 expression could account for refractory HR versus MR GBM findings. The Cancer Genome Atlas (TCGA) uses expression profiling to ascribe “proneural,” “classical,” and “mesenchymal” sub-type identities across an extensive panel of bulk GBM tissue samples (Brennan et al., 2013). However, as shown (Figures S3B and S3C), these subtypes were not predictive of infection. Expression of neural stem cell markers SOX2 and MSI-1, as well as surface receptors Integrin  $\alpha v \beta 5$  and AXL, is associated with ZIKV permissivity (Chavali et al., 2017; Chen et al., 2018; Garcez et al., 2016; Retallack et al., 2016; Souza et al., 2016; Zhu et al., 2017, 2020). These genes were highly expressed in the tumors analyzed, but we found no correlation between the level of bulk tissue expression and infection levels (Figure 3C).

Although such cell-intrinsic expression features of GBM progenitors did not account for rates of ZIKV infection, we observed that HR GBM segregated both from MR GBM and HDB based on innate immune system signature genes such as *human leucocyte antigen (HLA)*, *CD74*, *IBA1*, *CD45*, and *CD11b*, a marker of myeloid lineage (Figures 3C and S3D). Indeed, deconvolution analysis identified a glioma myeloid cell signature, which was strongest in HR GBM (Figure S3E). We used IF and smFISH to confirm that IBA1+ and RUNX1+ myeloid cell populations were increased in the HR GBM slices and dissociated cultures compared with MR GBM; indeed, myeloid cells were nearly undetectable in HDB (Figures 3D and S3D–S3F). Across the range of primary cultures assayed, bulk ZIKV-mCh+ fractions were enriched for expression of pro-inflammatory cytokines *IFNB1*, *IFNL1*, and *CCL5* when compared with ZIKV-mCh- fractions (Figure 3E). To validate these findings, we analyzed ZIKV infection and myeloid cell marker expression in primary slice cultures.

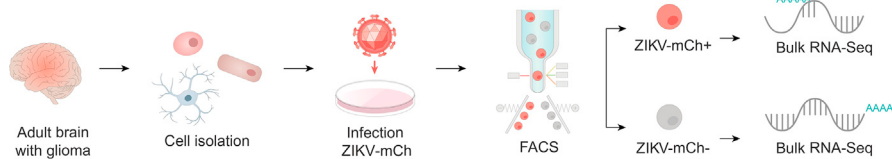
*RUNX1* expression was almost entirely absent in ZIKV-high HDB slices, whereas it was strongly enriched in HR GBM slices (Figure 3F). Some myeloid cell populations are vulnerable to ZIKV infection (Meertens et al., 2017; Quicke et al., 2016; Wang et al., 2018; Xu et al., 2020), but there is also evidence that monocyte-derived macrophages can effectively restrict intrinsic Zika replication (Yang et al., 2021). Therefore, the close correlation observed between tissue myeloid cell content and ZIKV-refractory behavior in our models invited closer analysis of the interactions of glioma cells with myeloid cells and their effects on infection dynamics.

To this end, we performed single-cell RNA-seq (scRNA-seq) of ZIKV-mCh+ FACS-purified cells from six primary GBM samples (Figure 4A). These data showed expression of the virus reporter across the range of glioma cell subtypes and in myeloid cells, the sole ZIKV-mCh+ immune cell population identified (Figures S4A–S4C). The proportion of myeloid cells was over-represented in HR GBM samples versus MR GBM (Figure 4B), and we noted that proneural GBM cell identities (oligodendrocyte progenitor cell [OPC]-like and neural progenitor cell [NPC]-like) distinguished MR GBM compared with HR GBM libraries (Figure S4D;  $\chi^2 = 34.1$  p < 0.0001) (Neftel et al., 2019). We next amalgamated scRNA-seq data from each patient cell fraction into “pseudo-bulk” RNA-seq libraries (Squair et al., 2021), allowing comparison of ZIKV levels using a DE-Seq2 model incorporating cell autonomous (glioma cell subtype) and microenvironment (MR GBM versus HR GBM) determinants. Despite the apparent trend to higher virus levels in proneural (oligodendrocyte precursor cell-like and neural progenitor cell-like) glioma cell subtypes (Figure 4C), overall no significant association between glioma cell subtype and ZIKV read count was demonstrated (DE-Seq2, p > 0.05 all pairwise comparisons). On the other hand, cell fractions from MR GBM tumors demonstrated significantly higher ZIKV read counts compared with HR GBMs ( $\log_{2}fc = 2.51$ , p < 0.0001). Furthermore, ZIKV read counts were significantly higher in SOX2-expressing ZIKV-mCh+ cells than in those without SOX2 reads (Figure S4E). ZIKV read counts were lowest of all in ZIKV-mCh+ myeloid cells themselves (Figure 4D). The latter is consistent with recent findings that myeloid cells can internalize oncolytic herpes simplex virus and express reporter genes without supporting viral replication (Delwar et al., 2018). Whereas snap-frozen uninfected GBM controls demonstrated a broad range of myeloid cell identity states (Sankowski et al., 2019), ZIKV-mCh+ myeloid cells exhibited exclusively pro-inflammatory anti-viral states (Figure 4E). Taken together, we conclude that variation in ZIKV levels between HR and MR GBM-derived glioma cells (Figure 4D) greatly exceeds that

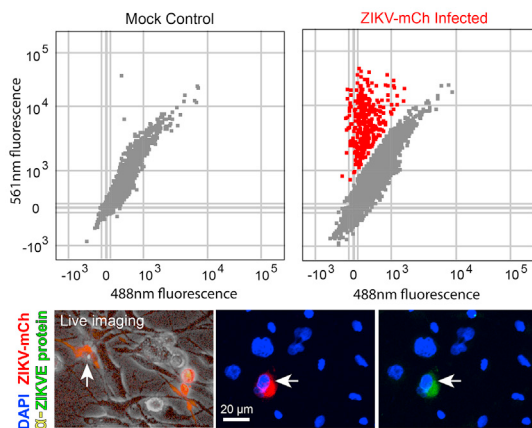
**Figure 2. SOX2+ target cell composition alone cannot account for HDB/GBM ZIKV infection/resistance**

- (A) Primary HDB and GBM tissue was subject to enzymatic dissociation followed by plating in serum-free adherent culture. Representative IF of key lineage markers in primary HDB and GBM dissociated adherent cultures is shown (see also Figure S2C).
- (B) Representative IF (left) and RT-qPCR (right) of 6 HDB and 20 GBM dissociated adherent cultures. Highly refractory and moderately refractory GBM cultures were defined with reference to the median ZIKV copy number for all GBMs analyzed (ZIKV MOI:1 48 h and ZIKV MOI:3 72 h, respectively). Each RT-qPCR data point represents the average copy number across three replicate wells/slices per sample. (Mann-Whitney test \*\*\* p < 0.001, \*\*\*\* p < 0.0001). Mean values for each category are indicated by horizontal lines.
- (C) Representative IF (left) and % cells SOX2+ in HDB (n = 4 specimens), HR GBM (n = 4 patients), and MR GBM (n = 4 patients) adherent cultures (left) and cell counts for IF and smFISH are determined by manual counting of at least 200 cells per condition. Mean values across all biological replicates for each condition are indicated by horizontal lines. (ANOVA p < 0.0001 across all three distributions).

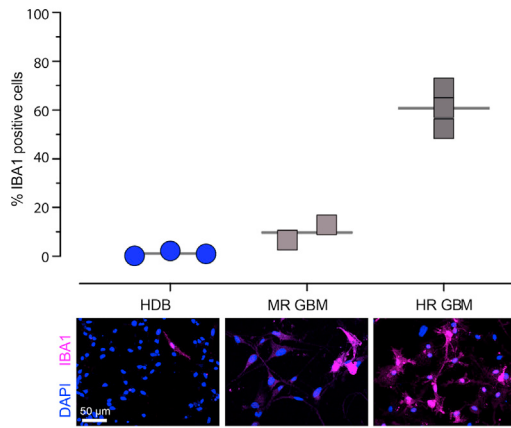
**A ZIKV-mCh Bulk RNA-Sequencing Workflow**



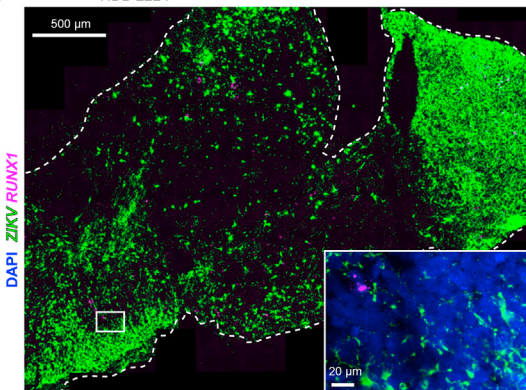
**B FACS using ZIKV-mCh Reporter Expression**



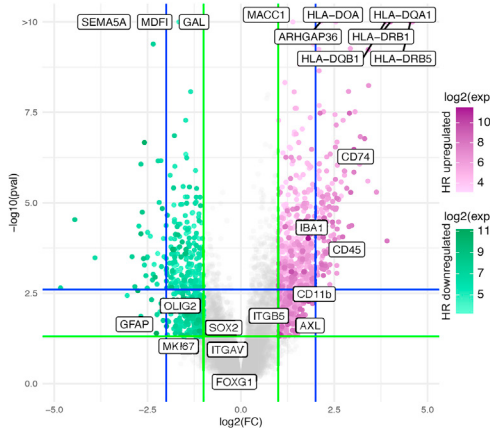
**D Myeloid cell content - dissociated primary cultures**



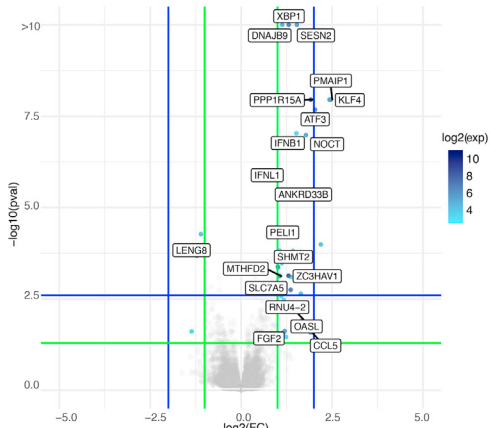
**F HDB 2224**



**C Differential expression: HR GBM vs MR GBM**



**E GBM ZIKV-mCh+ vs ZIKV-mCh-**



(legend on next page)

associated with proneural versus non-proneural cell identity (Figure 4C), again suggesting that tumor microenvironment (TME) rather than cell-intrinsic factors could be the key determinant of ZIKV progenitor cell infection.

### Tumor myeloid cells render GBM refractory to ZIKV infection

Findings above prompted us to directly test function of the myeloid cells over-represented in the HR GBM TME. We purified TME myeloid cells from primary GBM cultures ( $n = 7$  independent samples) using CD11b magnetic-activated cell sorting (MACS) (Figure 5A), which yielded live CD11b-positive GBM fractions (GBM11b+) enriched for a variety of IBA1+ myeloid cells (Figure S4F) and depleted for SOX2+ glioma cells, as well as CD11b-depleted GBM fractions (GBM11b−), exhibiting a higher SOX2/IBA1 ratio (Figures 5B and S5A) compared with parental GBM cultures.

We first analyzed productive ZIKV infection of the GBM11b+ fraction (i.e., TME myeloid cells alone) compared with the bulk parental GBM cells. As shown (Figure 5C), we found that RNA copies were significantly reduced in GBM11b+ fractions, indicating that myeloid cells were refractory to productive infection. Interestingly, GBM11b− fractions showed higher infection rates versus parental bulk GBM (Figure 5D), indicating that myeloid cell depletion enhanced productive infection. Third, we tested the ability of myeloid cells to drive the permissive GBM cell lines (E22, E34) to a ZIKV-refractory state (Figures 1F and S2A); we found that addition of GBM11b+ cells to GBM lines in a 1:2 ratio was associated with >10-fold reduction in ZIKV levels (Figures 5E, 5F, and S5B). Finally, TME myeloid cells also rendered primary HDB cultures ZIKV-refractory (Figure S5C), suggesting a neuroprotective effect.

### Myeloid-cell-secreted cytokines prevent progenitor cell ZIKV infection

We next investigated the molecular basis for non-cell autonomous myeloid cell-driven inhibition of glioma cell infection. To assay whether this mechanism involved secreted factors, we harvested filtered conditioned medium (CM) from the CD11b− and CD11b+ fractions of three primary GBM dissociated cell cultures and from GBM E22 and GBM E34 lines (11b−CM, 11b+CM, and LineCM, respectively; Figure 6A). Small volumes of conditioned media were also obtained from sorted HDB CD11b+ fractions for cytokine assay (Figure S5D). Application of 11b+CM to GBM E22, GBM E34, and HDB-FB1 cell lines resulted in an approximately 10-fold reduction in ZIKV levels compared with control LineCM treatment (Figure 6B).

We used RNA-seq to identify transcriptional changes in lines GBM E22, GBM E34, and primary HDB cells on treatment with 11b+CM. A total of 154 differentially expressed genes across these libraries were strongly enriched for interferon-stimulated genes (ISGs) by gene ontology analysis (Figure S5E). Furthermore, all 16 genes differentially expressed in the three cell lines were ISGs (Figure 6C). In contrast, expression of intrinsic “stemness” genes such as SOX2, OLIG2, and FOXG1 in glioma cells was unaffected by 11b+CM treatment (Figure S5F), giving no reason to suspect that interferon treatment at these levels compromises self-renewal or viability.

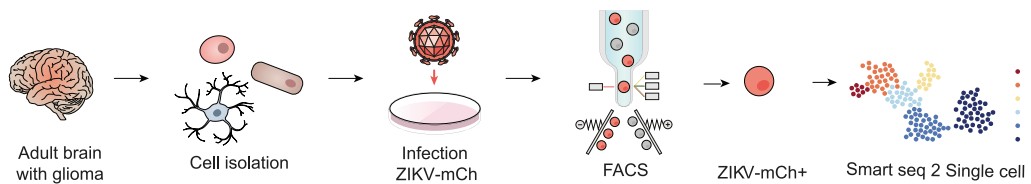
Analysis of 11b+CM samples by Meso Scale Discovery (MSD) assay indicated significant enrichment for 15 cytokines compared with paired 11b−CM samples ( $n = 4$  each; paired t tests) (Figure 6D). High levels of CXCL8, TNF- $\alpha$ , and IL-6, pro-inflammatory cytokines associated with intracellular pathogen killing and neutrophil recruitment (Dixit and Simon, 2012; Mantovani et al., 2004), would be predicted to contribute to anti-viral properties *in vivo*. The most striking fold-change enrichment in 11b+CM samples, however, was for anti-viral cytokines including IFN $\beta$ . We observed further enrichment for these factors in conditioned media harvested from (1) GBM11b+ and (2) HDB11b+ fractions pretreated with poly(I:C) to mimic the presence of viral RNA, denoting this poly(I:C)-responsive conditioned media Pi:c\_11b+CM (Figure 6E). Importantly, neither HDB nor GBM lines themselves were able to generate a comparable magnitude of secreted IFN $\beta$  response compared with myeloid cells (Figure 6E).

We extended analysis of ZIKV neuroprotective effects to HBD progenitors (Figure 7) and observed robust dose-dependent ability of recombinant IFN $\beta$  to inhibit ZIKV production at concentrations equivalent to those found in 11b+CM harvested with or without poly(I:C) stimulation (Figure 7A), whereas treatment with control recombinant cytokines also present at high levels in our conditioned media was associated with no effect (Figure S5G). IFN $\beta$  drives JAK/STAT signaling, and we found that addition of IFN $\beta$  or poly(I:C) 11b+CM drove dose-dependent phosphorylation of STAT1 in GBM cell lines (Figure 7B). In both lines, STAT1 phosphorylation was inhibited by the JAK1/2 inhibitor, ruxolitinib. Blunted or absent type 1 interferon responses have previously been reported in both pluripotent and tissue stem cell populations (Burke et al., 1978; Wu et al., 2018); hence, we next tested the ability of HDB cells and GBM lines to respond to IFN $\beta$ . In each case, a robust dose-dependent ISG response was evident (Figure 7C). Furthermore, pre-treatment of GBM E22 cells with IFN $\beta$  for 24 h prior to ZIKV exposure abolished infection as assessed by IF, with infection rates restored by

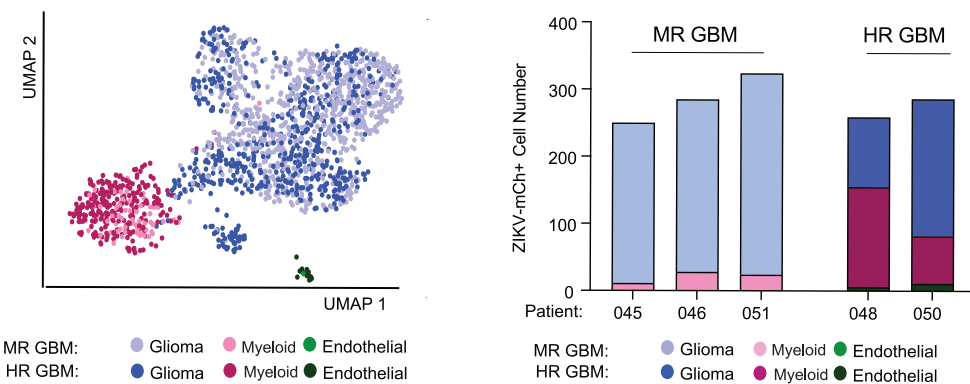
### Figure 3. RNA sequencing identifies an innate immune signature in ZIKV-refractory GBM

- (A) Experimental scheme: dissociated primary HDB and GBM cultures were infected with ZIKV-mCh reporter virus, then sorted by FACS into mCherry negative and positive fractions for sequencing as shown.
- (B) ZIKV-mCherry reporter (ZIKV-mCh) coincides with flavivirus envelope protein expression ( $\alpha$ -ZIKVE protein Sigma MAB10216), marking the ZIKV-infected fraction.
- (C) edgeR differential expression analysis of bulk RNA-seq in HR GBM ( $n = 3$  Cherry paired libraries) versus MR GBM ( $n = 4$  Cherry positive/negative paired libraries). Key glioma cell and myeloid cell signature genes are highlighted. HLA-class II antigen-presenting genes and myeloid cell markers are highlighted.
- (D) Cell counts and representative IF images for myeloid cell marker IBA1 in dissociated cell cultures ( $n = 3$  each). Mean values are indicated by horizontal lines.
- (E) edgeR differential expression ZIKV-mCh+ versus ZIKV-mCh− primary GBM culture fractions.
- (F) ZIKV-infected HDB and GBM slice cultures: smFISH for ZIKV and myeloid cell marker RUNX1.

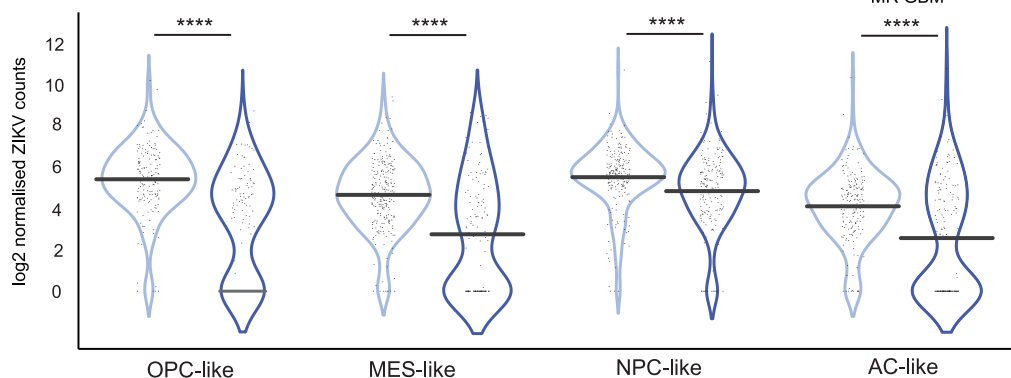
**A Smart-Seq2 single cell RNA-Sequencing Workflow**



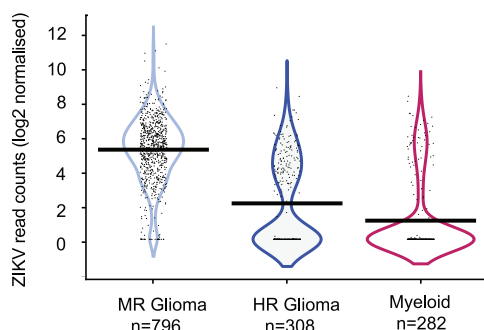
**B ZIKV-mCh+ Single cell clustering and cell-type composition of MR/HR ZIKV-mCh+ fractions**



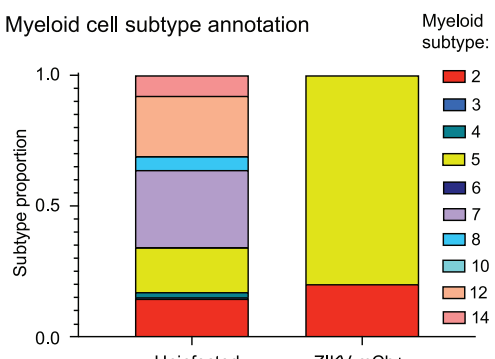
**C Per Cell ZIKV Read Counts in GBM MR and HR ZIKV-mCh+ glioma cells by subtype** — HR GBM — MR GBM



**D ZIKV-mCh+ Glioma cell subtype distribution**



**E Myeloid cell subtype annotation**



(legend on next page)

addition of ruxolitinib (Figure S5H). Likewise, RT-qPCR confirmed near total inhibition of productive ZIKV infection in both HDB and GBM lines on pre-treatment with Pi:c\_11b+CM or IFN $\beta$ , and conversely, infection was partially or completely restored by the addition of ruxolitinib under these conditions (Figure 7D). Finally, we tested primary HDB explants to investigate the neuroprotective effects of IFN $\beta$  against ZIKV. As shown (Figure 7E), IFN $\beta$  treatment reduced infection of SOX2+ progenitors.

## DISCUSSION

We cross-compared ZIKV infection rates in human primary samples of HDB versus patient GBM to better understand the determinants of neurotropic infection in normal and malignant progenitor populations. Our findings reveal a common regulatory role for the human myeloid secretome and a potent neuroprotective effect of IFN $\beta$  against ZIKV for HDB progenitors cells. This work has special relevance, given the history of ZIKV epidemic microcephaly in low- and middle-income countries, and the possibility of new epidemic ZIKV variants (Regla-Nava et al., 2022).

In this study, we used human models to avoid the caveats of interspecies limitations that are especially marked in the fields of ZIKV infection, GBM biology, and myeloid identity states (Gorman et al., 2018; Oh et al., 2014; Sankowski et al., 2019). For example, infection of mouse central nervous system cells typically requires a genetic background of *Ifn1b* loss of function and/or mouse-adapted virus strains (Gorman et al., 2018; Lazear et al., 2016; Geirsdottir et al., 2019). Although we cannot exclude some degree of *in vitro* artefact, there is ample clinical evidence for high infectability of HDB, captured faithfully in our primary slice culture experiments. It is therefore reasonable to assume that culture conditions do not materially impair tissue permissivity to ZIKV in GBM. In fact, over time, in slice culture, we would expect SOX2+ glioma cells to outgrow the differentiated myeloid fraction and perhaps become more susceptible to Zika; however, within the timeframe of our experiments (up to 7 days), we did not observe such a tendency. Instead, we found that SOX2+ progenitors in GBM were refractory to ZIKV infection relative to HDB SOX2+ progenitors and that this property derived from non-contact mediated effects of myeloid cells.

### A common myeloid pathway regulates ZIKV infection of human developing brain and malignant neural progenitors

Our findings indicate the myeloid cell secretome regulates resilience against ZIKV infection of developing and malignant hu-

man neural progenitors. Although such progenitors share a common transcriptional identity (Bulstrode et al., 2017; Ligon et al., 2007; Suvà et al., 2014), we observed that HDB tissue was markedly more permissive to ZIKV infection compared with GBM. Although GBM virus RNA levels in this study were similar to those previously reported ( $\sim$ 1,000–1,500 viral genome copies per ng RNA) (Zhu et al., 2020), direct comparison to HDB tissue in this study reveals the dramatic relative extent of refractory ZIKV infection in GBM. Interrogating tropism at the single-cell level indicated only mildly enhanced infection of proneural (neural progenitor cell-like and oligodendrocyte precursor cell-like) glioma cell subtypes compared with astrocyte-like and mesenchymal-like glioma cells (Neftel et al., 2019). Across the ZIKV-mCh+ GBM single cells analyzed, the presence of SOX2 transcripts was associated with higher ZIKV read counts, in keeping with an established role for SOX2 in driving ZIKV target cell identity (Zhu et al., 2020). Conversely, we found a strong correlation of HDB and GBM sample myeloid cell signatures with ZIKV resistance. Although the few myeloid cells present in HDB can themselves support ZIKV infection (Retallack et al., 2016; Wang et al., 2018; Xu et al., 2020), we found that GBM myeloid cells do not allow the virus to reproduce, as previously reported for oncolytic herpes simplex virus (Delwar et al., 2018). We speculate that this difference could reflect either functional immaturity of myeloid cells in the developing brain or cell origin, since bone marrow-derived macrophages rather than brain microglia can represent the majority myeloid population in GBM (Buonfiglioli and Hambardzumyan, 2021). Importantly, our study highlights the contribution of the myeloid secretome in the regulation of GBM resistance to ZIKV. We observed that GBM myeloid cells secreted a variety of both pro- and anti-inflammatory cytokines, which may reflect a diversity of activation states at baseline. However, single-cell analysis demonstrated that ZIKV-mCh+-selected myeloid cells converged on primarily pro-inflammatory anti-viral transcriptomic signatures (Sankowski et al., 2019).

### Myeloid secretion of IFN $\beta$ renders GBM refractory to ZIKV

In keeping with prior studies addressing stem cell anti-viral responses (Burke et al., 1978; Wu et al., 2018, 2019), we found that GBM and HDB neural progenitors exhibited limited capacity to produce interferons themselves in response to exposure to viral mimetic poly(I:C). Treatment with exogenous recombinant IFN $\beta$  (or myeloid conditioned medium) conferred ZIKV resistance as well as a signature of downstream JAK-STAT signaling in GBM lines. The JAK1/2 inhibitor ruxolitinib (Quintás-Cardama

**Figure 4. ZIKV productively infects diverse glioma stem cell identities**

Infection is modulated by TME myeloid cells, and these adopt pro-inflammatory anti-viral states in response to ZIKV-mCh+ uptake.  
(A) Plate-based Smart-Seq2 single-cell analysis of FACS sorted ZIKV-mCh+ GBM cells demonstrates predominance of glioma cell and myeloid cell identities.  
(B) Proportions of each cell type captured in 3 MR GBM and 2 HR GBM ZIKV-mCh+ single-cell libraries.  
(C) Per cell normalized ZIKV read counts by glioma cell subtype: oligodendrocyte precursor cell-like (OPC-like), mesenchymal-like (MES-like), neural precursor cell-like (NPC-like), astrocyte-like (AC-like) (Neftel et al., 2019), and by parent tumor ZIKV resistance for all ZIKV-mCh+ glioma cells captured (horizontal bar indicates mean normalized transcript count per cell). \*\*\* p < 0.00001 Wilcoxon signed rank test for all cell subtype GBM MR versus HR comparisons.  
(D) Summary per cell normalized ZIKV read counts for ZIKV-mCh+ glioma cells in MR and HR GBM, and for myeloid cells from all tumors pooled (horizontal bar indicates mean normalized transcript count per cell; Wilcoxon-signed rank test glioma cell [HR GBM] versus glioma cell [MR GBM] p =  $8.3 \times 10^{-64}$ ).  
(E) Myeloid cell transcriptional subtypes comprising uninfected parent tumor samples (profiled by 10x RNA-seq) and ZIKV-mCh+ myeloid cells (Smart-Seq2). Clusters according to Sankowski et al. (2019): clusters 2 and 5 correspond to pro-inflammatory anti-viral states.

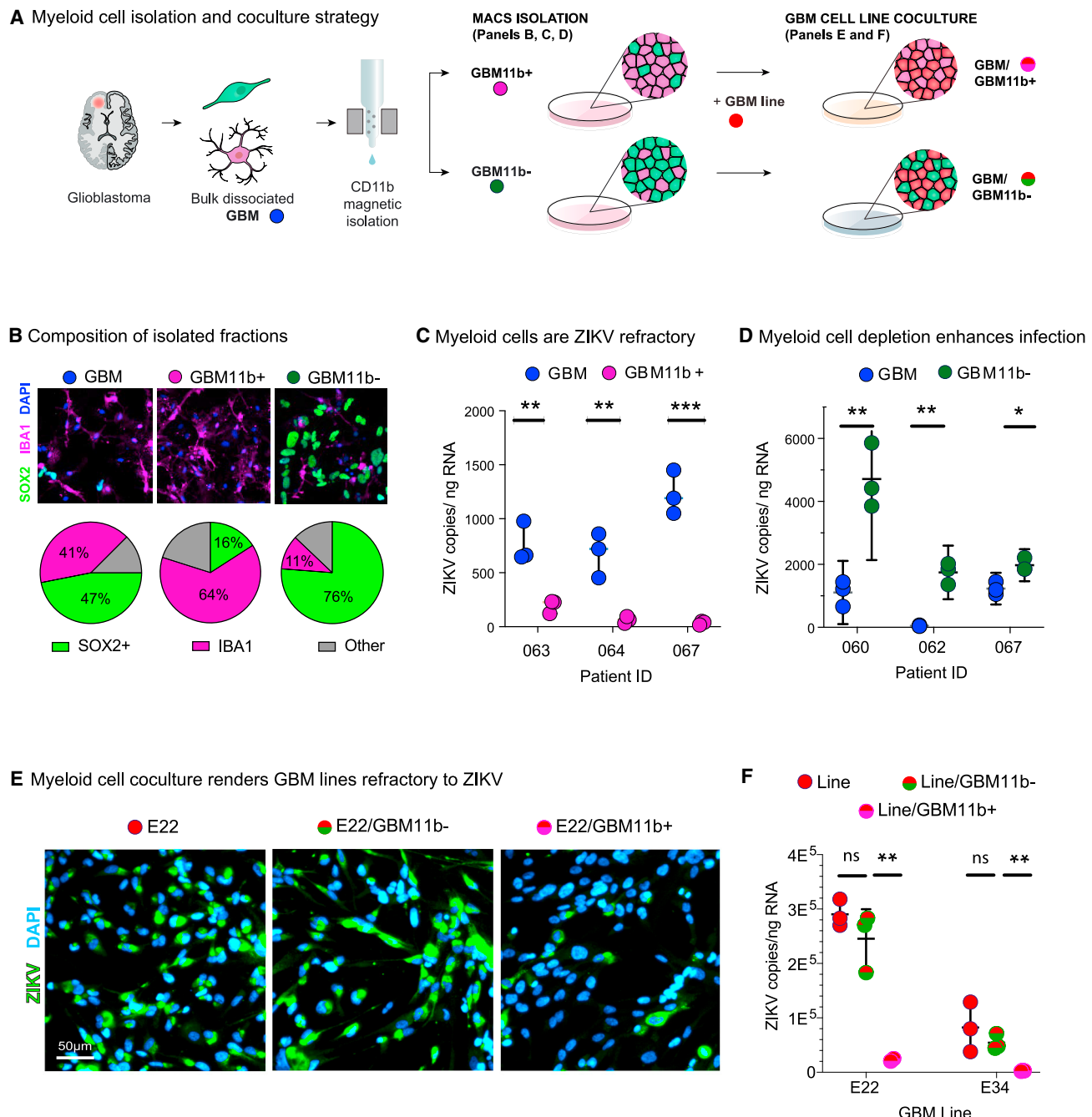


**Figure 5. Glioma myeloid cells confer ZIKV resistance**

(A) Primary GBM samples were dissociated to single-cell suspension and plated in bulk (GBM), or first separated into CD11b-enriched (GBM11b+) and CD11b-deplete fractions (GBM11b-) using antibody-conjugated magnetic bead and column-based sorting. These fractions were assayed directly or in coculture with HDB and GBM lines.

(B) Representative IF images of SOX2+ glioma cells and IBA1+ myeloid cells in GBM, GBM11b+, and GBM11b- fractions, and average proportion of each cell type across n = 4 matched bulk and sorted GBM fractions.

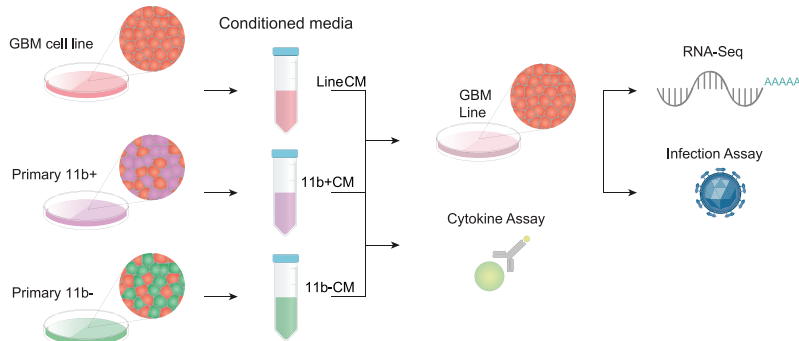
(C) ZIKV PE243 copy number assayed by RT-qPCR in paired infected GBM and GBM11b+ primary cultures (n = 3).

(D) ZIKV PE243 copy number assayed by RT-qPCR in paired infected GBM and GBM11b- primary cultures (n = 3).

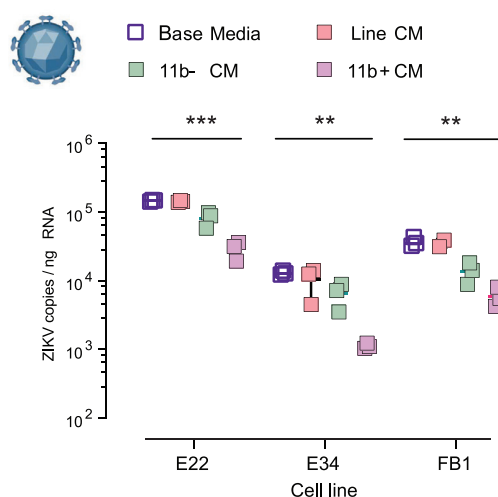
(E) GBM E22 line infected in isolation or in coculture with GBM11b- or GBM11b+ fractions at a 2:1 ratio, then fixed at 48 hpi for IF (see also Figure S5).

(F) GBM E22 line infected in isolation or in coculture with GBM11b- or GBM11b+ fractions, processed for RNA extraction and RT-qPCR viral copy number assay. For (C,D and F), mean and SD are shown, statistical tests are all unpaired t test \* p < 0.05; \*\* p < 0.01; \*\*\* p < 0.001; ns, not significant (see also Figure S5).

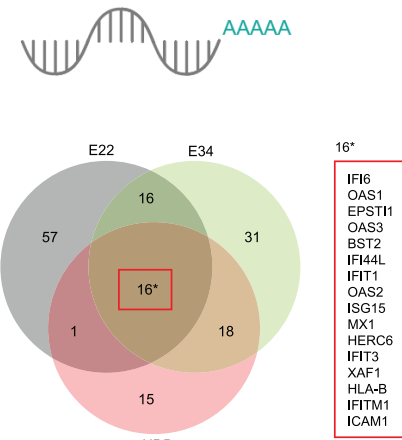
**A Conditioned Media (CM) Assay of Myeloid cell Secretome and Effects**



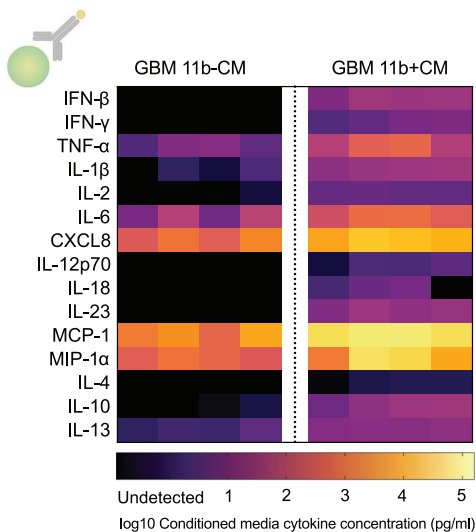
**B 11b+ Conditioned media confers ZIKV resistance**



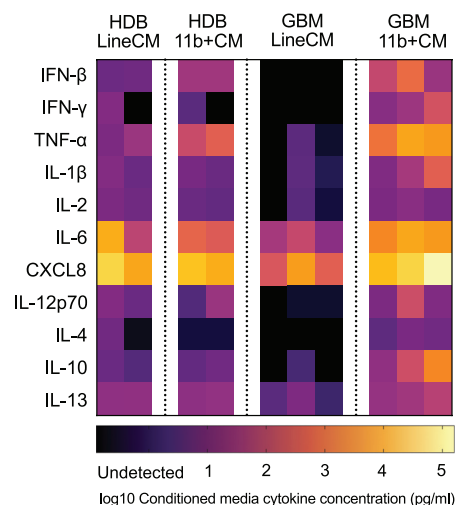
**C Upregulated on 11b+ Conditioned Media Treatment**



**D Secretome untreated**



**E Secretome following Poly(i:c) stimulation**



(legend on next page)

et al., 2010) almost completely restored ZIKV infection in GBM lines despite treatment with myeloid cell conditioned media (11b+CM) or IFN $\beta$ , whereas in HDB lines, ruxolitinib-induced rescue was incomplete, suggesting that other cytokines present could also be involved. Therapeutic targeting of the myeloid cell secretome could present clinically treatment possibilities in conjunction with ZIKV (Pyonteck et al., 2019). For example, our study suggests enhanced killing of GBM progenitors by ZIKV when given with inhibitors of type 1 interferon (e.g., IFNAR1 blocking antibody anifrolumab) (Peng et al., 2015), TYK2 inhibitor deucravacitinib (Papp et al., 2018), and/or inhibitors of JAK-STAT signaling such as ruxolitinib (Quintás-Cardama et al., 2010), which could be delivered with virus locally to the tumor resection cavity to minimize systemic side effects.

### HDB neural progenitors can be protected against ZIKV by the myeloid secretome or treatment with IFN $\beta$

Our results agree with prior findings that myeloid cells in HDB are sparsely distributed and morphologically immature in first trimester HDB, coinciding with the greatest vulnerability to Zika congenital syndrome (Andjelkovic et al., 1998). We speculate that the paucity and/or functional immaturity of myeloid cells at early stages of human brain development could underlie devastating congenital neuropathology due to ZIKV in particular and TORCH infections more widely, but further research is needed (Megli and Coyne, 2021). Our findings indicate that developing and malignant neural progenitors depend on myeloid cell-secreted type 1 interferons for effective ZIKV resistance. RNA-seq data revealed no differential expression of neural “stemness” markers after myeloid cell-CM treatment in either HDB or GBM lines, indicating that myeloid cells can induce a potent anti-viral response in these populations without changing their identity or progeny outputs. Indeed, type 1 interferon is administered clinically for treatment of viral hepatitis, myeloproliferative disorders, and multiple sclerosis among others, and available data in women exposed during pregnancy suggest no increased incidence of adverse fetal outcomes (Hellwig et al., 2020; Zhang et al., 2021).

### STAR★METHODS

Detailed methods are provided in the online version of this paper and include the following:

- KEY RESOURCES TABLE
- RESOURCE AVAILABILITY
  - Lead contact

### Figure 6. Glioma myeloid cells drive Zika resistance through cytokine secretion

- (A) Conditioned media harvested from GBM11b+ fractions (11b+CM), from GBM11b– fractions (11b–CM), and from GBM lines (LineCM), profiled using Meso Scale Discovery U-Plex and V-Plex (MSD) cytokine panels, and applied to GBM lines for conditioned media functional assays and expression profiling.
- (B) ZIKV RT-qPCR 48 h post infection (MOI = 1) of GBM lines GBM E22 and GBM E34 and HDB FB1 cells cultured in base media, LineCM, 11b–CM, or 11b+CM (two-way ANOVA cell line contribution  $p < 0.0001$  and conditioned media contribution  $p < 0.0001$ ; Welch's t test base media versus 11b+CM \*\*\*  $p < 0.001$ , \*\*  $p < 0.01$ ).
- (C) Venn diagram summarizes pattern of gene upregulation in GBM E22, GBM E34, and primary HDB cells (specimen BRC 2251) post-treatment with 11b+CM versus control LineCM.
- (D) MSD assay of cytokine content in 11b–CM and 11b+CM at 48 h in culture ( $n = 4$  paired GBM sample fractions from 4 patient tumors).
- (E) MSD assay of Pi:c-LineCM and Pi:c-11b+CM derived from the HDB and GBM fractions indicated, following stimulation with poly(I:C) viral dsRNA mimetic at 10  $\mu$ g/mL.

- Materials availability

- Data and code availability

### ● EXPERIMENTAL MODEL AND SUBJECT DETAILS

- Primary human tissue
- Primary GBM and HDB slice culture
- Primary dissociated adherent cell culture
- Cell lines

### ● METHOD DETAILS

- Magnetic-activated cell sorting (MACS isolation)
- ZIKV preparation
- ZIKV titration
- ZIKV infection
- Conditioned media collection and experiments
- IFN $\beta$  and ruxolitinib experiments
- Western blotting
- Immunofluorescence (IF) for dissociated adherent cells
- Immunofluorescence for GBM and HDB slices
- smFISH (RNAscope) sample preparation
- smFISH and IF automated imaging and analysis
- Zika viral RNA quantification
- RNA extraction, library preparation and sequencing
- Bulk RNA-Seq Analysis
- CIBERSORT Analysis
- Single cell RNA-Seq analysis

### ● QUANTIFICATION AND STATISTICAL ANALYSIS

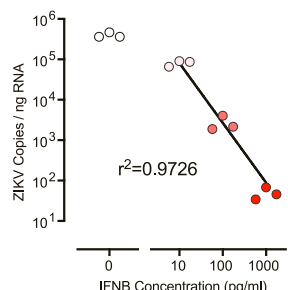
### SUPPLEMENTAL INFORMATION

Supplemental information can be found online at <https://doi.org/10.1016/j.neuron.2022.09.002>.

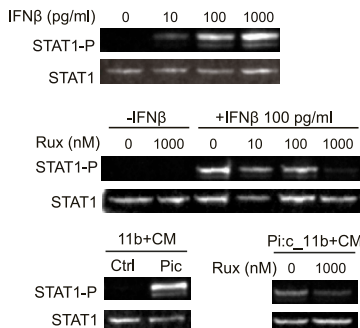
### ACKNOWLEDGMENTS

We would like to thank the members of the Rowitch, Gergely, Sweeney, Morhorianu, Barker, Bayraktar, and Franklin labs for their valuable technical help and especially Clare Bryant for helpful comments and suggestions. Flow cytometry including sorting of live ZIKV-mCh-infected cells was performed by the NIHR Cambridge Biomedical Research Centre Cell Phenotyping Hub. Meso Scale Discovery assays were performed by the NIHR Cambridge Biomedical Research Centre, Core Biochemistry Assay Laboratory. GBM cell lines were provided by the Glioma Cellular Genetics Resource ([www.gcgr.org.uk](http://www.gcgr.org.uk)). H.B. acknowledges the support of his NIHR Clinical Lecturer post and of the University of Cambridge Division of Neurosurgery. Funding: Cancer Research UK Pioneer Award A24423 (H.B.), Wellcome Career Development Fellowship 223011/Z/21/Z (H.B.), Cancer Research UK C14303/A17197 and A24455 (F.G.), Dr. Miriam and Sheldon G Adelson Medical Research Foundation (D.H.R.), European Research Council Advanced Grant, GA no. 789054 (D.H.R.), Wellcome Trust Investigator Award 88114 (D.H.R.), Wellcome Trust/Royal Society Sir Henry Dale Fellowship award 202471/Z/16/Z (T.R.S.), Biotechnology and Biological Sciences Research Council

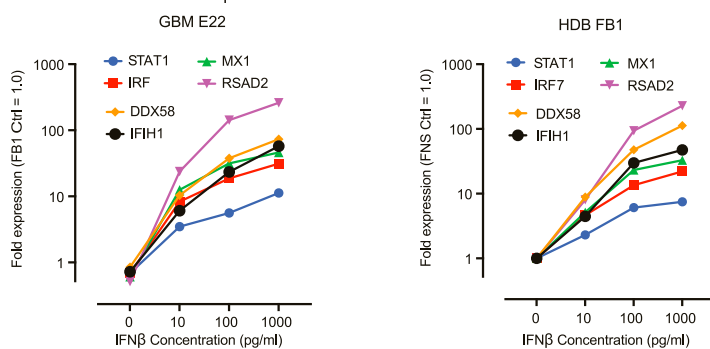
**A** GBM E22 exogenous type 1 interferon response



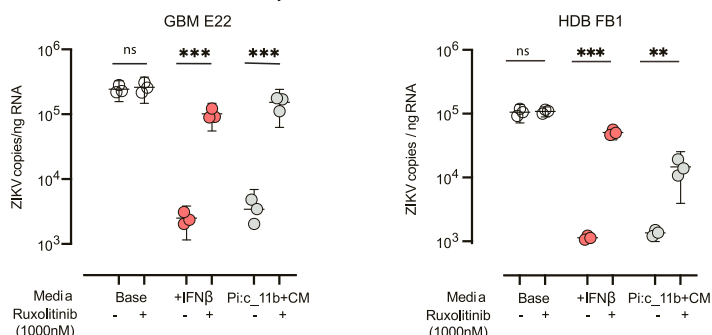
**B** JAK/STAT Response to IFNB/CM



**C** Interferon Stimulated Gene Responses in GBM and HDB lines



**D** Induction and reversal of ZIKV resistance by Interferon/JAK/STAT modulation



**E** Induction of ZIKV resistance by IFNβ in HDB slice culture

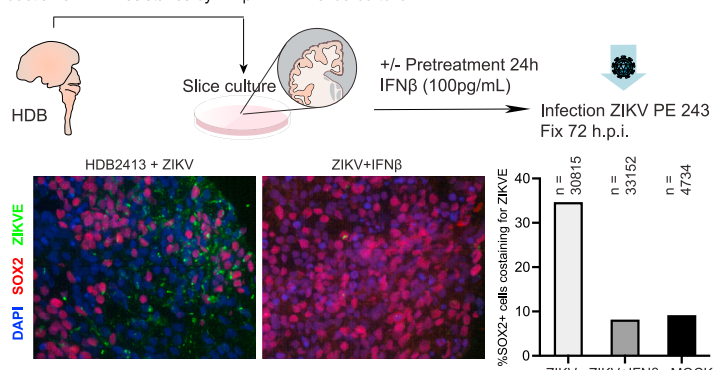


**Figure 7. Myeloid-cell-secretome-induced resistance reflects IFNβ content and can be reversed by JAK/STAT inhibition**

(A) ZIKV RT-qPCR of GBM E22 cultures 48 hpi treated with exogenous recombinant IFNβ as indicated.

(B) STAT1 phosphorylation in GBM E22 cells harvested 3 h post-treatment with: (upper) recombinant IFNβ, (middle) IFNβ ± JAK1/2 inhibitor ruxolitinib, and (lower) 11b+CM and Pi:c-11b+CM ± ruxolitinib (Rux).

(C) Normalized expression by qRT-PCR for the interferon-stimulated genes indicated in GBM E22 and HDB FB1 cultures, in response to exogenous IFNβ at the indicated media concentrations, normalized to GAPDH expression and with gene expression in untreated HDB FB1 cells assigned the value 1.0. (D) ZIKV RT-qPCR in HDB FB1 (left) and GBM E22 glioma stem cells (right) 48 hpi or 48 h with or without 24 h pre-treatment with IFNβ (100 pg/mL) or Pi:c-11b+CM, ± ruxolitinib 1,000 nM (unpaired t test \*\* p < 0.01, \*\*\* p < 0.001; ns, not significant).

(E) HDB slice cultures harvested at 72 hpi, infected with ZIKV ± IFNβ. Graph shows the percentage of SOX2+ cells infected with ZIKV versus total SOX2+ cells for the conditions indicated, MOCK is uninfected. n is the total cells analyzed across 3 slices per condition, 1–3 replicate cryosections per slice, in 1 HDB sample.

BBS/E/I/00007031 (T.R.S.), Cancer Research UKA21922 (GCG lines: S.M.P.), Chan-Zuckerberg Initiative Pediatric Cell Atlas, NIHR Cambridge Biomedical Research Centre BRC-1215-20014 (D.H.R.). Views expressed are those of the authors and not necessarily those of the NIHR or the Department of Health and Social Care.

#### AUTHOR CONTRIBUTIONS

Conceptualization: H.B., D.H.R., F.G., A.M.H.Y., G.C.G., and T.G. Methodology: H.B., G.C.G., T.G., A.M.H.Y., T.F., T.R.S., J.H.S., and E.J.H. Investigation: H.B., G.C.G., T.G., C.H., and D.M.F. GBM collection and processing: H.B., G.C.G., D.M.F., A.J., R. Morris, R. Mair, C.W., T.R.S., and S.J.P. HDB collection and processing: H.B., G.C.G., X.H., and R.A.B. ZIKV workflows: T.G., H.B., T.F., D.M.F., and T.R.S. Image analysis: G.C.G., K.R., Z.X., and H.B. Experimental analysis: H.B., G.C.G., and T.G. Bioinformatic analysis: I. Moutsopoulos, I. Mohorianu, A.A., O.B., and H.B. Data curation: H.B., I. Moutsopoulos, I. Mohorianu, A.A., and O.B. Visualization: H.B., G.C.G., T.G., I. Moutsopoulos, I. Mohorianu, A.A., and O.B. Project administration: H.B., D.H.R., F.G., G.C.G., and T.G. Funding acquisition: H.B., D.H.R., and F.G. Supervision: D.H.R., F.G., S.M.P., and P.J.A.H. Writing: H.B., D.H.R., F.G., G.C.G., and T.G., contributions of all authors.

#### DECLARATION OF INTERESTS

The authors declare no competing interests.

Received: June 4, 2022

Revised: August 10, 2022

Accepted: September 1, 2022

Published: September 28, 2022

#### REFERENCES

- Andjelkovic, A.V., Nikolic, B., Pachter, J.S., and Zecevic, N. (1998). Macrophages/microglial cells in human central nervous system during development: an immunohistochemical study. *Brain Res.* 814, 13–25. [https://doi.org/10.1016/s0006-8993\(98\)00830-0](https://doi.org/10.1016/s0006-8993(98)00830-0).
- Andrews, S. (2010). FastQC: a quality control tool for high throughput sequence data. <http://www.bioinformatics.babraham.ac.uk/projects/fastqc/>.
- Bao, S., Wu, Q., McLendon, R.E., Hao, Y., Shi, Q., Hjelmeland, A.B., Dewhirst, M.W., Bigner, D.D., and Rich, J.N. (2006). Glioma stem cells promote radiosensitivity by preferential activation of the DNA damage response. *Nature* 444, 756–760. <https://doi.org/10.1038/nature05236>.
- Bolstad, B.M., Irizarry, R.A., Åstrand, M., and Speed, T.P. (2003). A comparison of normalization methods for high density oligonucleotide array data based on variance and bias. *Bioinformatics* 19, 185–193. <https://doi.org/10.1093/bioinformatics/19.2.185>.
- Brennan, C.W., Verhaak, R.G.W., McKenna, A., Campos, B., Noushmehr, H., Salama, S.R., Zheng, S., Chakravarty, D., Sanborn, J.Z., Berman, S.H., et al. (2013). The somatic genomic landscape of glioblastoma. *Cell* 155, 462–477. <https://doi.org/10.1016/j.cell.2013.09.034>.
- Bulstrode, H., Johnstone, E., Marques-Torrejon, M.A., Ferguson, K.M., Bressan, R.B., Blin, C., Grant, V., Gogolok, S., Gangoso, E., Gagrica, S., et al. (2017). Elevated FOXG1 and SOX2 in glioblastoma enforces neural stem cell identity through transcriptional control of cell cycle and epigenetic regulators. *Genes Dev.* 31, 757–773. <https://doi.org/10.1101/gad.293027.116>.
- Buonfiglioli, A., and Hambardzumyan, D. (2021). Macrophages and microglia: the cerberus of glioblastoma. *Acta Neuropathol. Commun.* 9, 54. <https://doi.org/10.1186/s40478-021-01156-z>.
- Burke, D.C., Graham, C.F., and Lehman, J.M. (1978). Appearance of interferon inducibility and sensitivity during differentiation of murine teratocarcinoma cells in vitro. *Cell* 13, 243–248. [https://doi.org/10.1016/0092-8674\(78\)90193-9](https://doi.org/10.1016/0092-8674(78)90193-9).
- Carod-Artal, F.J. (2018). Neurological complications of Zika virus infection. *Expert Rev. Anti. Infect Ther.* 16, 399–410. <https://doi.org/10.1080/14787210.2018.1466702>.
- Chavali, P.L., Stojic, L., Meredith, L.W., Joseph, N., Nahorski, M.S., Sanford, T.J., Sweeney, T.R., Krishna, B.A., Hosmillo, M., Firth, A.E., et al. (2017). Neurodevelopmental protein Musashi-1 interacts with the Zika genome and promotes viral replication. *Science* 357, 83–88. <https://doi.org/10.1126/science.aam9243>.
- Chen, Q., Wu, J., Ye, Q., Ma, F., Zhu, Q., Wu, Y., Shan, C., Xie, X., Li, D., Zhan, X., et al. (2018). Treatment of human glioblastoma with a live attenuated Zika virus vaccine candidate. *mBio* 9, e01683-18. <https://doi.org/10.1128/mBio.01683-18>.
- Cugola, F.R., Fernandes, I.R., Russo, F.B., Freitas, B.C., Dias, J.L.M., Guimarães, K.P., Benazzato, C., Almeida, N., Pignatari, G.C., Romero, S., et al. (2016). The Brazilian Zika virus strain causes birth defects in experimental models. *Nature* 534, 267–271. <https://doi.org/10.1038/nature18296>.
- Delwar, Z.M., Kuo, Y., Wen, Y.H., Rennie, P.S., and Jia, W. (2018). Oncolytic virotherapy blockade by microglia and macrophages requires STAT1/3. *Cancer Res.* 78, 718–730. <https://doi.org/10.1158/0008-5472.CAN-17-0599>.
- Dixit, N., and Simon, S.I. (2012). Chemokines, selectins and intracellular calcium flux: temporal and spatial cues for leukocyte arrest. *Front. Immunol.* 3, 188. <https://doi.org/10.3389/fimmu.2012.00188>.
- Dobin, A., Davis, C.A., Schlesinger, F., Drenkow, J., Zaleski, C., Jha, S., Batut, P., Chaisson, M., and Gingeras, T.R. (2013). STAR: ultrafast universal RNA-seq aligner. *Bioinformatics* 29, 15–21. <https://doi.org/10.1093/bioinformatics/bts635>.
- Donald, C.L., Brennan, B., Cumberworth, S.L., Rezelj, V.V., Clark, J.J., Cordeiro, M.T., Freitas de Oliveira França, R., Pena, L.J., Wilkie, G.S., Da Silva Filipe, A., et al. (2016). Full genome sequence and sfRNA interferon antagonist activity of Zika virus from Recife, Brazil. *PLoS Negl. Trop. Dis.* 10, e0005048. <https://doi.org/10.1371/journal.pntd.0005048>.
- Ewels, P., Magnusson, M., Lundin, S., and Käller, M. (2016). MultiQC: summarize analysis results for multiple tools and samples in a single report. *Bioinformatics* 32, 3047–3048. <https://doi.org/10.1093/bioinformatics/btw354>.
- Fajardo, T., Sanford, T.J., Mears, H.V., Jasper, A., Storrie, S., Mansur, D.S., and Sweeney, T.R. (2020). The flavivirus polymerase NS5 regulates translation of viral genomic RNA. *Nucleic Acids Res.* 48, 5081–5093. <https://doi.org/10.1093/nar/gkaa242>.
- Fleming, S.J., Marioni, J.C., and Babadi, M. (2019). CellBender remove-background: a deep generative model for unsupervised removal of background noise from scRNA-seq datasets. <https://doi.org/10.1101/791699>.
- Gangoso, E., Southgate, B., Bradley, L., Rus, S., Galvez-Cancino, F., McGivern, N., Güç, E., Kapourani, C.A., Byron, A., Ferguson, K.M., et al. (2021). Glioblastomas acquire myeloid-affiliated transcriptional programs via epigenetic immunoediting to elicit immune evasion. *Cell* 184, 2454.e26–2470.e26. <https://doi.org/10.1016/j.cell.2021.03.023>.
- Garcez, P.P., Loiola, E.C., Madeiro da Costa, R.M. da, Higa, L.M., Trindade, P., Delvecchio, R., Nascimento, J.M., Brindeiro, R., Tanuri, A., and Rehen, S.K. (2016). Zika virus impairs growth in human neurospheres and brain organoids. *Science* 352, 816–818. <https://doi.org/10.1126/science.aaf6116>.
- Geirsdottir, L., David, E., Keren-Shaul, H., Weiner, A., Bohlen, S.C., Neuber, J., Balic, A., Giladi, A., Sheban, F., Dutertre, C.-A., et al. (2019). Cross-species single-cell analysis reveals divergence of the primate microglia program. *Cell* 179, 1609.e16–1622.e16. <https://doi.org/10.1016/j.cell.2019.11.010>.
- Gimple, R.C., Bhargava, S., Dixit, D., and Rich, J.N. (2019). Glioblastoma stem cells: lessons from the tumor hierarchy in a lethal cancer. *Genes Dev.* 33, 591–609. <https://doi.org/10.1101/gad.324301.119>.
- Gorman, M.J., Caine, E.A., Zaitsev, K., Begley, M.C., Weger-Lucarelli, J., Uccellini, M.B., Tripathi, S., Morrison, J., Yount, B.L., Dinnon, K.H., et al. (2018). An immunocompetent mouse model of Zika virus infection. *Cell Host Microbe* 23, 672.e6–685.e6. <https://doi.org/10.1016/j.chom.2018.04.003>.
- Harrington, K., Freeman, D.J., Kelly, B., Harper, J., and Soria, J.-C. (2019). Optimizing oncolytic virotherapy in cancer treatment. *Nat. Rev. Drug Discov.* 18, 689–706. <https://doi.org/10.1038/s41573-019-0029-0>.
- Hellwig, K., Geissbuehler, Y., Sabidó, M., Popescu, C., Adamo, A., Klinger, J., Ornoy, A., and Huppke, P.; European Interferon-beta Pregnancy Study Group

- (2020). Pregnancy outcomes in interferon-beta-exposed patients with multiple sclerosis: results from the European interferon-beta Pregnancy Registry. *J. Neurol.* 267, 1715–1723. <https://doi.org/10.1007/s00415-020-09762-y>.
- Kruger, F. (2012). A wrapper tool around Cutadapt and FastQC to consistently apply quality and adapter trimming to FastQ files, with some extra functionality for Mspl-digested RRBS-type (reduced representation bisulfite-seq) libraries. [https://www.bioinformatics.babraham.ac.uk/projects/trim\\_galore/](https://www.bioinformatics.babraham.ac.uk/projects/trim_galore/).
- Lazear, H.M., Govero, J., Smith, A.M., Platt, D.J., Fernandez, E., Miner, J.J., and Diamond, M.S. (2016). A mouse model of Zika virus pathogenesis. *Cell Host Microbe* 19, 720–730. <https://doi.org/10.1016/j.chom.2016.03.010>.
- Li, H., Saucedo-Cuevas, L., Regla-Nava, J.A., Chai, G., Sheets, N., Tang, W., Terskikh, A.V., Shresta, S., and Gleeson, J.G. (2016). Zika virus infects neural progenitors in the adult mouse brain and alters proliferation. *Cell Stem Cell* 19, 593–598. <https://doi.org/10.1016/j.stem.2016.08.005>.
- Liao, Y., Smyth, G.K., and Shi, W. (2014). featureCounts: an efficient general purpose program for assigning sequence reads to genomic features. *Bioinformatics* 30, 923–930. <https://doi.org/10.1093/bioinformatics/btt656>.
- Ligon, K.L., Huillard, E., Mehta, S., Kesari, S., Liu, H., Alberta, J.A., Bachoo, R.M., Kane, M., Louis, D.N., Depinho, R.A., et al. (2007). Olig2-regulated lineage-restricted pathway controls replication competence in neural stem cells and malignant glioma. *Neuron* 53, 503–517. <https://doi.org/10.1016/j.neuron.2007.01.009>.
- Liu, Y.-P., Suksanpaisan, L., Steele, M.B., Russell, S.J., and Peng, K.-W. (2013). Induction of antiviral genes by the tumor microenvironment confers resistance to virotherapy. *Sci. Rep.* 3, 2375. <https://doi.org/10.1038/srep02375>.
- Love, M.I., Huber, W., and Anders, S. (2014). Moderated estimation of fold change and dispersion for RNA-seq data with DESeq2. *Genome Biol.* 15, 550. <https://doi.org/10.1186/s13059-014-0550-8>.
- Mantovani, A., Sica, A., Sozzani, S., Allavena, P., Vecchi, A., and Locati, M. (2004). The chemokine system in diverse forms of macrophage activation and polarization. *Trends Immunol.* 25, 677–686. <https://doi.org/10.1016/j.it.2004.09.015>.
- McCarthy, D.J., Chen, Y., and Smyth, G.K. (2012). Differential expression analysis of multifactor RNA-seq experiments with respect to biological variation. *Nucleic Acids Res.* 40, 4288–4297. <https://doi.org/10.1093/nar/gks042>.
- Meertens, L., Labeau, A., Dejarnac, O., Cipriani, S., Sinigaglia, L., Bonnet-Madin, L., Le Charpentier, T.L., Hafirassou, M.L., Zamborlini, A., Cao-Lormeau, V.M., et al. (2017). Axl mediates ZIKA virus entry in human glial cells and modulates innate immune responses. *Cell Rep.* 18, 324–333. <https://doi.org/10.1016/j.celrep.2016.12.045>.
- Megli, C.J., and Coyne, C.B. (2021). Infections at the maternal–fetal interface: an overview of pathogenesis and defence. *Nat. Rev. Microbiol.* 20, 67–82. <https://doi.org/10.1038/s41579-021-00610-y>.
- Mehta, S., Huillard, E., Kesari, S., Maire, C.L., Golebiowski, D., Harrington, E.P., Alberta, J.A., Kane, M.F., Theisen, M., Ligon, K.L., et al. (2011). The central nervous system-restricted transcription factor Olig2 opposes p53 responses to genotoxic damage in neural progenitors and malignant glioma. *Cancer Cell* 19, 359–371. <https://doi.org/10.1016/j.ccr.2011.01.035>.
- Mohorianu, I., Bretman, A., Smith, D.T., Fowler, E.K., Dalmary, T., and Chapman, T. (2017). Comparison of alternative approaches for analysing multi-level RNA-seq data. *PLoS One* 12, e0182694. <https://doi.org/10.1371/journal.pone.0182694>.
- Moutsopoulos, I., Maischak, L., Lauzikaite, E., Vasquez Urbina, S.A., Williams, E.C., Drost, H.-G., and Mohorianu, I.I. (2021). noisyR: enhancing biological signal in sequencing datasets by characterizing random technical noise. *Nucleic Acids Res.* 49, e83. <https://doi.org/10.1093/nar/gkab433>.
- Muffat, J., Li, Y., Omer, A., Durbin, A., Bosch, I., Bakiasi, G., Richards, E., Meyer, A., Gehrke, L., and Jaenisch, R. (2018). “Human induced pluripotent stem cell-derived glial cells and neural progenitors display divergent responses to Zika and dengue infections.”. *Proc Natl Acad Sci.* 3;115, 7117–7122. <https://doi.org/10.1073/pnas.1719266115>.
- Mutso, M., Saul, S., Rausalu, K., Susova, O., Žusinaite, E., Mahalingam, S., and Merits, A. (2017). Reverse genetic system, genetically stable reporter viruses and packaged subgenomic replicon based on a Brazilian Zika virus isolate. *J. Gen. Virol.* 98, 2712–2724. <https://doi.org/10.1099/jgv.0.000938>.
- Neftel, C., Laffy, J., Filbin, M.G., Hara, T., Shore, M.E., Rahme, G.J., Richman, A.R., Silverbush, D., Shaw, M.L., Hebert, C.M., et al. (2019). An integrative model of cellular states, plasticity, and genetics for glioblastoma. *Cell* 178, 835.e21–849.e21. <https://doi.org/10.1016/j.cell.2019.06.024>.
- Newman, A.M., Liu, C.L., Green, M.R., Gentles, A.J., Feng, W., Xu, Y., Hoang, C.D., Diehn, M., and Alizadeh, A.A. (2015). Robust enumeration of cell subsets from tissue expression profiles. *Nat. Methods* 12, 453–457. <https://doi.org/10.1038/nmeth.3337>.
- Oh, T., Fakurnejad, S., Sayegh, E.T., Clark, A.J., Ivan, M.E., Sun, M.Z., Safaei, M., Bloch, O., James, C.D., and Parsa, A.T. (2014). Immunocompetent murine models for the study of glioblastoma immunotherapy. *J. Transl. Med.* 12, 107. <https://doi.org/10.1186/1479-5876-12-107>.
- Papp, K., Gordon, K., Thaçi, D., Morita, A., Gooderham, M., Foley, P., Grgis, I.G., Kundu, S., and Banerjee, S. (2018). Phase 2 trial of selective tyrosine kinase 2 inhibition in psoriasis. *N. Engl. J. Med.* 379, 1313–1321. <https://doi.org/10.1056/NEJMoa1806382>.
- Peng, L., Oganesyan, V., Wu, H., Dall'Acqua, W.F., and Damschroder, M.M. (2015). Molecular basis for antagonistic activity of anifrolumab, an anti-interferon- $\alpha$  receptor 1 antibody. *mAbs* 7, 428–439. <https://doi.org/10.1080/19420862.2015.1007810>.
- Polański, K., Park, J.-E., Young, M.D., Miao, Z., Meyer, K.B., and Teichmann, S.A. (2019). BBKNN: fast batch alignment of single cell transcriptomes. *Bioinformatics* 36, 964–965. <https://doi.org/10.1093/bioinformatics/btz625>.
- Pyontek, S.M., Akkari, L., Schuhmacher, A.J., Bowman, R.L., Sevenich, L., Quail, D.F., Olson, O.C., Quick, M.L., Huse, J.T., Teijeiro, V., et al. (2019). CSF-1R inhibition alters macrophage polarization and blocks glioma progression. *Nat. Med.* 19, 1264–1272. <https://doi.org/10.1038/nm.3337>.
- Quicke, K.M., Bowen, J.R., Johnson, E.L., McDonald, C.E., Ma, H., O’Neal, J.T., Rajakumar, A., Wrammert, J., Rimawi, B.H., Pulendran, B., et al. (2016). Zika virus infects human placental macrophages. *Cell Host Microbe* 20, 83–90. <https://doi.org/10.1016/j.chom.2016.05.015>.
- Quintás-Cardama, A., Vaddi, K., Liu, P., Mansouri, T., Li, J., Scherle, P.A., Caulder, E., Wen, X., Li, Y., Waeltz, P., et al. (2010). Preclinical characterization of the selective JAK1/2 inhibitor INCB018424: therapeutic implications for the treatment of myeloproliferative neoplasms. *Blood* 115, 3109–3117. <https://doi.org/10.1182/blood-2009-04-214957>.
- Raudvere, U., Kolberg, L., Kuzmin, I., Arak, T., Adler, P., Peterson, H., and Vilo, J. (2019). g:profiler: a web server for functional enrichment analysis and conversions of gene lists (2019 update). *Nucleic Acids Res.* 47, W191–W198. <https://doi.org/10.1093/nar/gkz369>.
- Regla-Nava, J.A., Wang, Y.T., Fontes-Garfias, C.R., Liu, Y., Syed, T., Susantono, M., Gonzalez, A., Viramontes, K.M., Verma, S.K., Kim, K., et al. (2022). A Zika virus mutation enhances transmission potential and confers escape from protective dengue virus immunity. *Cell Rep.* 39, 110655. <https://doi.org/10.1016/j.celrep.2022.110655>.
- Retallack, H., Di Lullo, E., Arias, C., Knopp, K.A., Laurie, M.T., Sandoval-Espinosa, C., Mancia Leon, W.R., Krencik, R., Ullian, E.M., Spatazza, J., et al. (2016). Zika virus cell tropism in the developing human brain and inhibition by azithromycin. *Proc. Natl. Acad. Sci. USA* 113, 14408–14413. <https://doi.org/10.1073/pnas.1618029113>.
- Sankowski, R., Böttcher, C., Masuda, T., Geirsdottir, L., Sagar, Sindram, E., Seredenina, T., Muhs, A., Scheiwe, C., Shah, M.J., et al. (2019). Mapping microglia states in the human brain through the integration of high-dimensional techniques. *Nat. Neurosci.* 22, 2098–2110. <https://doi.org/10.1038/s41593-019-0532-y>.
- Souza, B.S.F., Sampaio, G.L.A., Pereira, C.S., Campos, G.S., Sardi, S.I., Freitas, L.A.R., Figueira, C.P., Paredes, B.D., Nonaka, C.K.V., Azevedo, C.M., et al. (2016). Zika virus infection induces mitosis abnormalities and apoptotic cell death of human neural progenitor cells. *Sci. Rep.* 6, 39775. <https://doi.org/10.1038/srep39775>.

- Squair, J.W., Gautier, M., Kathe, C., Anderson, M.A., James, N.D., Hutson, T.H., Hudelle, R., Qaiser, T., Matson, K.J.E., Barraud, Q., et al. (2021). Confronting false discoveries in single-cell differential expression. *Nat. Commun.* 12, 5692. <https://doi.org/10.1038/s41467-021-25960-2>.
- Stuart, T., Butler, A., Hoffman, P., Hafemeister, C., Papalexi, E., Mauck, W.M., Hao, Y., Stoeckius, M., Smibert, P., and Satija, R. (2019). Comprehensive integration of single-cell data. *Cell* 177, 1888.e21–1902.e21. <https://doi.org/10.1016/j.cell.2019.05.031>.
- Sturm, D., Bender, S., Jones, D.T.W., Lichter, P., Grill, J., Becher, O., Hawkins, C., Majewski, J., Jones, C., Costello, J.F., et al. (2014). Paediatric and adult glioblastoma: multiform (epi)genomic culprits emerge. *Nat. Rev. Cancer* 14, 92–107. <https://doi.org/10.1038/nrc3655>.
- Suvà, M.L., Rheinbay, E., Gillespie, S.M., Patel, A.P., Wakimoto, H., Rabkin, S.D., Riggi, N., Chi, A.S., Cahill, D.P., Nahed, B.V., et al. (2014). Reconstructing and reprogramming the tumor-propagating potential of glioblastoma stem-like cells. *Cell* 157, 580–594. <https://doi.org/10.1016/j.cell.2014.02.030>.
- Suvà, M.L., and Tirosh, I. (2020). The glioma stem cell model in the era of single-cell genomics. *Cancer Cell* 37, 630–636.
- Tang, H., Hammack, C., Ogden, S.C., Wen, Z., Qian, X., Li, Y., Yao, B., Shin, J., Zhang, F., Lee, E.M., et al. (2016). Zika virus infects human cortical neural progenitors and attenuates their growth. *Cell Stem Cell* 18, 587–590. <https://doi.org/10.1016/j.stem.2016.02.016>.
- Viteri, G., Matthews, L., Varusai, T., Gillespie, M., Milacic, M., Cook, J., Weiser, J., Shorser, S., Sidiropoulos, K., Fabregat, A., et al. (2019). Reactome and ORCID—fine-grained credit attribution for community curation. *Database (Oxford)* 2019, baz123. <https://doi.org/10.1093/database/baz123>.
- Wang, J., Liu, J., Zhou, R., Ding, X., Zhang, Q., Zhang, C., and Li, L. (2018). Zika virus infected primary microglia impairs NPCs proliferation and differentiation. *Biochem. Biophys. Res. Commun.* 497, 619–625. <https://doi.org/10.1016/j.bbrc.2018.02.118>.
- Wang, Z., Sun, D., Chen, Y.-J., Xie, X., Shi, Y., Tabar, V., Brennan, C.W., Bale, T.A., Jayewickreme, C.D., Laks, D.R., et al. (2020). Cell lineage-based stratification for glioblastoma. *Cancer Cell* 38, 366.e8–379.e8. <https://doi.org/10.1016/j.ccr.2020.06.003>.
- Wegner, M., and Stolt, C.C. (2005). From stem cells to neurons and glia: a Soxist's view of neural development. *Trends Neurosci.* 28, 583–588. <https://doi.org/10.1016/j.tins.2005.08.008>.
- Wolf, F.A., Angerer, P., and Theis, F.J. (2018). SCANPY: large-scale single-cell gene expression data analysis. *Genome Biol.* 19, 15. <https://doi.org/10.1186/s13059-017-1382-0>.
- Wolock, S.L., Lopez, R., and Klein, A.M. (2019). Scrublet: computational identification of cell doublets in single-cell transcriptomic data. *Cell Syst.* 8, 281.e9–291.e9. <https://doi.org/10.1016/j.cels.2018.11.005>.
- Wu, X., Dao Thi, V.L.D., Huang, Y., Billerbeck, E., Saha, D., Hoffmann, H.-H., Wang, Y., Silva, L.A.V., Sarbanes, S., Sun, T., et al. (2018). Intrinsic immunity shapes viral resistance of stem cells. *Cell* 172, 423.e25–438.e25. <https://doi.org/10.1016/j.cell.2017.11.018>.
- Wu, X., Kwong, A.C., and Rice, C.M. (2019). Antiviral resistance of stem cells. *Curr. Opin. Immunol.* 56, 50–59. <https://doi.org/10.1016/j.co.2018.10.004>.
- Xu, P., Shan, C., Dunn, T.J., Xie, X., Xia, H., Gao, J., Allende Labastida, J.A., Zou, J., Villarreal, P.P., Schlagal, C.R., et al. (2020). Role of microglia in the dissemination of Zika virus from mother to fetal brain. *PLoS Negl. Trop. Dis.* 14, e0008413. <https://doi.org/10.1371/journal.pntd.0008413>.
- Yang, D., Chu, H., Lu, G., Shuai, H., Wang, Y., Hou, Y., Zhang, X., Huang, X., Hu, B., Chai, Y., et al. (2021). STAT2-dependent restriction of Zika virus by human macrophages but not dendritic cells. *Emerg. Microbes Infect.* 10, 1024–1037. <https://doi.org/10.1080/22221751.2021.1929503>.
- Zhang, M., Fu, S., Ren, D., Wu, Y., Yao, N., Ni, T., Feng, Y., Chen, Y., Chen, T., Zhao, Y., and Liu, J. (2021). Maternal and fetal outcomes after interferon exposure during pregnancy: a systematic review with meta-analysis. *Front. Reprod. Health* 3, 702929. <https://doi.org/10.3389/frph.2021.702929>.
- Zhang, Q., and Liu, F. (2020). Advances and potential pitfalls of oncolytic viruses expressing immunomodulatory transgene therapy for malignant gliomas. *Cell Death Dis.* 11, 1–11. <https://doi.org/10.1038/s41419-020-2696-5>.
- Zhu, Z., Gorman, M.J., McKenzie, L.D., Chai, J.N., Hubert, C.G., Prager, B.C., Fernandez, E., Richner, J.M., Zhang, R., Shan, C., et al. (2017). Zika virus has oncolytic activity against glioblastoma stem cells. *J. Exp. Med.* 214, 2843–2857. <https://doi.org/10.1084/jem.20171093>.
- Zhu, Z., Mesci, P., Bernatchez, J.A., Gimple, R.C., Wang, X., Schafer, S.T., Wettersten, H.I., Beck, S., Clark, A.E., Wu, Q., et al. (2020). Zika virus targets glioblastoma stem cells through a SOX2-integrin  $\alpha v \beta 5$  axis. *Cell Stem Cell* 26, 187.e10–204.e10. <https://doi.org/10.1016/j.stem.2019.11.016>.

## STAR★METHODS

### KEY RESOURCES TABLE

REAGENT or RESOURCE	SOURCE	IDENTIFIER
<b>Antibodies</b>		
Rabbit polyclonal anti IBA-1 (Wako)	Alpha Laboratories	Cat#019-19741; RRID: AB_839504
Goat polyclonal anti-Human SOX2	R & D Systems	Cat#AF201; RRID: AB_355110
Mouse monoclonal anti-Flavivirus Group Antigen, clone D1-4G2-4-15	Millipore Sigma	Cat#MAB10216; RRID: AB_827205
Rabbit monoclonal anti-Flavivirus Group Antigen, clone D1-4G2-4-15	Absolute Antibody	Cat#Ab00230-2.0; RRID: AB_2715504
Mouse monoclonal anti-Human Nestin (Clone 196908)		Cat#MAB1259; RRID: AB_2251304
Rabbit polyclonal anti-OLIG2	Millipore Sigma	Cat#AB9610; RRID: AB_570666
Rat monoclonal anti-GFAP (2.2B10)	ThermoFisher Scientific	Cat#13-0300; RRID: AB_2532994
Mouse monoclonal anti-Tuj1 Neuron-specific beta-III tubulin	Millipore Sigma	Cat#MAB1195; RRID: AB_357520
Rabbit monoclonal anti-Ki67 (SP6)	Abcam	Cat#ab16667; RRID: AB_302459
Mouse monoclonal Recombinant Anti-Ki67 [37C7-12]	Abcam	Cat#ab245113; RRID: AB_2923193
Rat monoclonal anti-MSI-1	MBL	Cat#D270-3; RRID: AB_1953023
Rabbit polyclonal anti-Cleaved Caspase 3 (Asp175)	Cell Signalling	Cat#9661S; RRID: AB_2341188
Mouse monoclonal anti-Pax6	DSHB	Cat# pax6, RRID: AB_528427
Rabbit polyclonal anti-CUX2	Abcam	Cat#ab216588; RRID: AB_442208
Goat polyclonal anti-SOX10	R & D Systems	Cat#AF2864; RRID: AB_442208
Rabbit monoclonal anti-PU.1	Cell Signalling	Cat#2258S; RRID: AB_2186909
Rabbit recombinant monoclonal anti-CD11b	Abcam	Cat#ab184308; RRID: AB_2889154
Rabbit polyclonal anti-TMEM119	Abcam	Cat#ab185333; RRID: AB_2687894
Goat clonal anti-IBA1	Abcam	Cat#ab5076; RRID: AB_2224402
Rabbit polyclonal anti-P2YR12	Atlas Antibodies (Sigma)	
Mouse monoclonal anti- STAT1	Cell Signalling	Cat#9176S; RRID: AB_10950970
Rabbit monoclonal anti-Phospho-Stat1 (Tyr701) (D4A7)	Cell Signalling	Cat#7649; RRID: AB_476692
Mouse monoclonal anti-β-Actin	Sigma Aldrich	Cat#A1978; RRID: AB_476692
Donkey polyclonal anti-Goat IgG (H+L) Cross-Adsorbed Secondary Antibody, Alexa Fluor 488	Life Technologies	Cat#A-11055; RRID: AB_2534102
Donkey polyclonal anti-Mouse IgG (H+L) Highly Cross-Adsorbed Secondary Antibody, Alexa Fluor 594	Life Technologies	Cat#A-21203; RRID: AB_141633
Polyclonal Donkey anti-Mouse IgG (H+L) Highly Cross-Adsorbed Secondary Antibody, Alexa Fluor 488	Life Technologies	Cat#A-21202; RRID: AB_141607
Donkey polyclonal anti-Rabbit IgG (H+L) Highly Cross-Adsorbed Secondary Antibody, Alexa Fluor 594	Life Technologies	Cat#A-21207; RRID: AB_141637
Donkey polyclonal anti-Mouse IgG (H+L) Highly Cross-Adsorbed Secondary Antibody, Alexa Fluor 647	Life Technologies	Cat#A-31571; RRID: AB_162542
Donkey polyclonal anti-Rabbit IgG (H+L) Highly Cross-Adsorbed Secondary Antibody, Alexa Fluor 647	Life Technologies	Cat#A-31573; RRID: AB_2536183
Goat polyclonal IRDye 680RD Goat Anti-Mouse IgG (H+L), 0.1 mg	LI-COR Biosciences	Cat#925-68070; RRID: AB_2651128
Goat polyclonal IRDye 680RD Goat Anti-Rabbit IgG (H+L), 0.1 mg	LI-COR Biosciences	Cat#925-68071; RRID: AB_2721181
Goat polyclonal IRDye 800CW Goat Anti-Rabbit IgG (H+L), 0.1 mg	LI-COR Biosciences	Cat#925-32211; RRID: AB_2651127

(Continued on next page)

***Continued***

REAGENT or RESOURCE	SOURCE	IDENTIFIER
Goat polyclonal IRDye 800CW Goat Anti-Mouse IgG (H+L), 0.1 mg	LI-COR Biosciences	Cat#925-32210; RRID: AB_2687825
Donkey polyclonal IRDye 680RD Donkey Anti-Goat IgG (H+L), 0.1 mg	LI-COR Biosciences	Cat#925-68074; RRID: AB_2650427
<b>Bacterial and virus strains</b>		
Zika PE243	A. Kohl, Centre for Virus Research, University of Glasgow	N/A
Zika-mCh	Fajardo et al., 2020	N/A
<b>Biological samples</b>		
Glioblastoma primary dissociated cells	REC 18/WM/0094 (Principal Investigator Harry Bulstrode); REC 18/EE/0172 (Principal Investigator Richard Mair) University of Cambridge/ Cambridge University Hospitals	GBM30,GBM31,GBM37,GBM39,GBM41, GBM42,GBM43,GBM45,GBM46,GBM47, GBM48,GBM50, GBM51,GBM53,GBM54, GBM55,GBM56,GBM57,GBM58,GBM59, GBM60,GBM62,GBM63,GBM66,GBM67, GBM68,GBM69,GBM70,GBM71,GBM72, GBM73,GBM74,GBM75
Glioblastoma primary tissue		GBM37,GBM42,GBM47, GBM67
Human developing brain dissociated cells	REC 96/085 (Principal Investigator Roger Barker) University of Cambridge/ Cambridge University Hospitals	HDB2196, HDB2208, HDB2223, HDB2215, HDB2225,HDB2226, HDB2233,HDB2229, HDB2251,HDB2279, HDB2285, HDB2293, HDB2413
Human developing brain primary tissue		HDB2208, HDB2224, HDB2225, HDB2413
<b>Critical commercial assays</b>		
RNeasy® Lipid Tissue mini Kit	Qiagen	Cat# 74804
Genesig Standard Zika Virus Quantification Kit, PrimerDesign	Genesig PrimerDesign	Path-ZIKV-standard
NEBNext® Ultra™ II Directional RNA Library Prep Kit for Illumina®	New England Biolabs	Cat# E7765
NEBNext Single Cell/Low Input RNA Library Prep Kit for Illumina	New England Biolabs	Cat# E6420L
Smartseq pico V2 library preparation (Ribosomal depletion)	Takara	Cat# 634442
<b>Deposited data</b>		
Bulk RNA-Sequencing data	Repository GSE178623	<a href="https://www.ncbi.nlm.nih.gov/geo/browse/">https://www.ncbi.nlm.nih.gov/geo/browse/</a>
Single cell RNA-Sequencing data	GSC Microglia Sanger S3 Storage database	<a href="https://gsc-microglia.cog.sanger.ac.uk/browser.html">https://gsc-microglia.cog.sanger.ac.uk/browser.html</a>
<b>Experimental models: Cell lines</b>		
HDB-FB1	Steve Pollard, Edinburgh ( <a href="http://gcgr.org.uk">gcgr.org.uk</a> )	Human Developing Forebrain, FNS1 – Forebrain
HDB-FB12	Steve Pollard, Edinburgh ( <a href="http://gcgr.org.uk">gcgr.org.uk</a> )	Human Developing Forebrain, FNS12 – Region 1
HDB-HB1	Steve Pollard, Edinburgh ( <a href="http://gcgr.org.uk">gcgr.org.uk</a> )	Human Developing Hindbrain. FNS1 - Hindbrain
HDB-HB12	Steve Pollard, Edinburgh ( <a href="http://gcgr.org.uk">gcgr.org.uk</a> )	Human Developing Hindbrain. FNS12 – Region 6
DMG 007	Angel Carcaboso, Barcelona	Diffuse Midline Glioma. HSJD-DIPG-007
DMG B117	Chris Jones, ICR London	Diffuse Midline Glioma, ICR-B117
DMG B169	Chris Jones, ICR London	Diffuse Midline Glioma, ICR-B169
GBM-E22	Steve Pollard, Edinburgh ( <a href="http://gcgr.org.uk">gcgr.org.uk</a> )	Glioblastoma, E22

(Continued on next page)

**Continued**

REAGENT or RESOURCE	SOURCE	IDENTIFIER
GBM-E25	Steve Pollard, Edinburgh ( <a href="http://gcgr.org.uk">gcgr.org.uk</a> )	Glioblastoma, E25
GBM-E34	Steve Pollard, Edinburgh ( <a href="http://gcgr.org.uk">gcgr.org.uk</a> )	Glioblastoma, E34
<b>smFISH probes</b>		
V-ZIKV Probe	N/A	ACD Cat# 467778
V-ZIKV Probe	N/A	ACD Cat# 467778-C4
V-ZIKA-pp-O3-sense-C2 Probe	GenBank: KJ776791.1	ACD Cat# 467911-C2
Hs-SOX2-C2 Probe	GenBank: NM_003106.3	ACD Cat# 400878
Hs-RUNX1-C3 Probe	GenBank: NM_001122607.1	ACD Cat# 419908-C3
Hs-RUNX1-C2 Probe	GenBank: NM_001122607.1	ACD Cat# 419908-C2
Hs-OLIG2-C2 Probe	GenBank: NM_005806.3	ACD Cat# 424198-C2
HS-DCX-C2 Probe	GenBank: NM_000555.3	ACD Cat# 489558-C2
HS-CD74 Probe	GenBank: NM_004355.3	ACD Cat# 477528
HS-CD44 Probe	GenBank: NM_000610	ACD Cat# 311278-C3
HS-SLC1A3 Probe	GenBank: NM_004172.4	ACD Cat# 461088
HS-PDGFRα Probe	GenBank: NM_006206.4	ACD Cat# 604488
RNAscope 4plex negative control Probe	N/A	ACD Cat# 321838
<b>Software and algorithms</b>		
FastQC (v0.11.8)	Andrews et al., 2010	N/A
MultiQC (v1.9)	Ewels et al., 2016	N/A
TrimGalore (v0.6.4_dev, based on cutadapt v3.4)	Kruger, 2012	N/A
STAR (v2.7.0a) with default parameters	Dobin et al., 2013	N/A
noisyR (v1.0.0) Moutsopoulos et al., 2021	Moutsopoulos et al., 2021	N/A
EdgeR (v3.34.0)	McCarthy et al., 2012	N/A
DESeq2 (v1.32.0)	Love et al., 2014	
g:profiler R package (v0.2.0)	Raudvere et al., 2019	( <a href="https://biit.cs.ut.ee/gprofiler/gost">https://biit.cs.ut.ee/gprofiler/gost</a> )
Reactome datasets	Viteri et al., 2019	N/A
CIBERSORT analysis pipeline	Newman et al., 2015	N/A
CellBender	Fleming et al., 2019	N/A
Scrublet algorithm	Wolock et al., 2019	N/A
BBKNN algorithm	Polański et al., 2019	N/A
CCA algorithm	Stuart et al., 2019	N/A
featureCounts (subread package, v2.0.0)	Liao et al., 2014	N/A
Prism v9.0.0	Graphpad Software LLC	N/A

## RESOURCE AVAILABILITY

### Lead contact

Further information and requests for resources and reagents should be directed to and will be fulfilled by the lead contact, David Rowitch ([dhr25@medsch.cam.ac.uk](mailto:dhr25@medsch.cam.ac.uk)).

### Materials availability

This study did not generate new unique reagents.

### Data and code availability

Single-cell and bulk RNA-seq data are publicly available as of the date of publication through Sanger Institute and GEO repositories respectively as detailed in the [key resources table](#). Accession numbers are listed in the [key resources table](#). Microscopy and Western blot data reported in this paper will be shared by the lead contact upon request.

This paper does not report original code.

Any additional information required to reanalyze the data reported in this paper is available from the lead contact upon request.

## EXPERIMENTAL MODEL AND SUBJECT DETAILS

### Primary human tissue

Patient GBM tissue was obtained with informed consent under UK Health Research Authority permissions REC 18/WM/0094 (Principal Investigator Harry Bulstrode), or REC 18/EE/0172 (Principal Investigator Richard Mair) and processed immediately following resection. Patient demographics and routine histopathological data are provided in [Table S2](#). The acquisition of HDB tissue was undertaken by Xiaoling He under provisions of UK Health Research Authority REC 96/085 (Principal Investigator Roger Barker). Gestational age data is provided in [Table S3](#), but no information on sex was available at these early developmental timepoints. Both patient GBM tissue and HDB tissue were processed under the provisions of REC 18/WM/0094 and in accordance with UK Human Tissue Authority regulations, and informed consent was obtained in all cases. GBM and HDB samples were either processed for dissociated cell culture and/or slice culture. In addition, small pieces of the sample were immediately fixed in 4% paraformaldehyde (PFA) overnight at 4 °C for later IF as T0 tissue, or snap frozen on OCT at -80 °C for nuc-RNA seq.

### Primary GBM and HDB slice culture

Diced tissue pieces 2–3-mm square were mounted in 4% low melting point agarose in DMEM. 350-µm slices were cut using a Leica (Wetzlar, Germany) VT1200 vibratome then transferred onto 0.4 µm organotypic inserts (Millipore/Sigma-Aldrich, PICM0RG50) in a 6 well plate containing 1ml per well of Slice culture maintenance media – Neurobasal (Life Technologies, 21103049) supplemented with 10mM HEPES, 1× B-27 supplement, 1× penicillin-streptomycin, and nystatin (6 U/mL, Sigma-Aldrich, N1638). The plate was then incubated for 3–5 days at 37 °C with regular media changes before ZIKV infection.

### Primary dissociated adherent cell culture

Tissue was diced in HBSS (Thermo Fisher Scientific, 14170112), spun for 5 min at 300g, and resuspended in activated Papain (Lorne, LS003126) in Hibernate A media (Thermo Fisher Scientific, A1370501). After 20 min (for HDB) or 45 min (for GBM) incubation at 37 °C, the tissue was spun down, and resuspended in isolation media (Hibernate A supplemented with FBS, 1x B-27, Insulin (Sigma-Aldrich, I9278, 4g/ml) and Sodium pyruvate (220g/ml)). The digested tissue was triturated using a glass pipette filtered over a 50 µm cell strainer into a 10% Percoll gradient (Sigma-Aldrich, GE17-5445-01) then spun for 20 min at 800 rcf (soft). The pellet was resuspended in 1ml red cell lysis buffer for 90 seconds. The reaction was stopped with DMEM/F-12 and spun for 5 min at 300g. Cells were either plated in flasks in NSC media or used for magnetic-activated cell sorting. Cells were either replated to 12 or 24 well plates for Zika infection up to 7 days post isolation, or frozen in NSC media + 10% DMSO 1-3 days after isolation.

NSC media was used for all dissociated cell culture, primary and GBM lines: DMEM/F12 (Gibco, 11320-033), supplemented with 15mM HEPES (Stock 1M, Sigma-Aldrich, H0887), D-Glucose (7.25ml of 100 g/L, Sigma, G8644), 1x MEM-NEAA (LifeTech/Gibco, 11140-035), 1x Pen-Strep (LifeTech/Gibco, 15140-122), BSA (800 µL of 7.5% LifeTech/Gibco, 15260-037), bMercETOH (100 µM, LifeTech/Gibco, 31350-010 (20ml), B27 (0.5x, LifeTech/Gibco, 17504-044), N2 (0.5x, LifeTech/Gibco, 17502-048), EGF (10ng/ml, Peprotech, 315-09-500), bFGF (10ng/ml, Peprotech, 100-18B-500), Laminin, (1µg/ml, Cultrex, 3446-005-01).

Glass plates were pre-coated with poly-L-ornithine (PLO) solution in PBS (10–15 µg/mL) at room temperature for 2 h. PLO solution was removed, plates washed twice with PBS, followed by a third wash with DMEM/F-12. Laminin was diluted in NSC media (20 µg/mL), added to PLO-coated glass plates or to plastic flasks/plates without PLO coating, and incubated at room temperature (15 – 25 °C) for at least 2 hours, then removed and fresh media added.

### Cell lines

GBM and HDB cell lines were generated and supplied from the Glioma Cellular Genetics Resource (gcgr.org.uk) with ethical approval from the NHS Health Research Authority (East of Scotland Research Ethics Service, REC reference 15/ES/0094). DMG cell lines were kindly provided by Angel Carcaboso and Chris Jones as indicated ([Table S4](#)). Cell lines were cultured in NSC media on laminin coated culture-ware at 37°C. Medium was changed every 3 days and cells were passaged using StemPro Accutase Cell Dissociation Reagent (Life Tech, A1110501). Cells were tested for mycoplasma regularly. No additional authentication was conducted on receipt of cell lines from the sources detailed.

## METHOD DETAILS

### Magnetic-activated cell sorting (MACS isolation)

To isolate myeloid cells from the primary bulk GBM single cell suspension, MACS was used following the manufacturer's instructions. A concentrated cell suspension was incubated with anti-CD11b conjugated magnetic beads (1:50, Miltenyi 130-049-601) for 15 min at 4 °C. Unbound beads were removed by dilution and spun down, then the cells resuspended in 1ml of Hibernate-A and passed through an MS column (Miltenyi, 130-042-201) on a magnetic stand. The flow-through was

collected as the GBM11b- fraction. The column-bound GBM11b+ population were subsequently eluted into a separate tube using Hibernate-A.

### ZIKV preparation

ZIKV PE243 stocks were generated by transfecting PE243 RNA (supplied by A. Kohl, Centre for Virus Research, University of Glasgow, Lindomar J. Pena and Rafael Oliveira de Freitas França, Fiocruz Recife, Pernambuco, Brazil) into Vero 2-2 cells using Lipofectamine 2000 (Life Technologies). Zika PE243 virus was amplified inoculating 100 µL of the rescued virus in 80-90% confluent flasks of Vero 2-2 cells. After 2-3 days, infected cell supernatants were pooled, centrifugated 10 min at 1,300 × g, 4°C and filtered through a 0.22 µm membrane. The pooled supernatant was supplemented with 10% glycerol then aliquoted in cryovials and stored at -80°C.

ZIKV-mCh production and titration was performed as previously described ([Fajardo et al., 2020](#)), based on a plasmid very generously shared by Andres Merits ([Mutso et al., 2017](#)), modified to incorporate T7 in place of SP6 promoter, also as previously described ([Fajardo et al., 2020](#)).

### ZIKV titration

Plaque forming assay was used to calculate viral titers (plaque forming units (PFU)/mL). Vero 2-2 cells were seeded in 6 well plates at density of  $1.5 \times 10^5$  cells/well and incubated at 5% CO<sub>2</sub>, 37 °C for 48 hours before infection. Serial dilutions of the viral stocks were made and then added to the Vero cells for 1 hour. Cells were covered with 2 mL Carboxy Methyl Cellulose overlay solution (CMC/DMEM) and further incubated for 5-7 days. CMC/DMEM overlay was washed with PBS and infected cells were fixed and stained for 30 min using a solution of crystal violet containing paraformaldehyde for plaque visualisation.

### ZIKV infection

Glioma cells and primary glioblastoma cells were seeded in 12 or 24 well plates at densities of  $3 \times 10^5$  or  $1.5 \times 10^5$  cells/well respectively and allowed to attach overnight. For later immunofluorescence, cells were plated in 8 well chamber slides, at a density of  $5 \times 10^4$  cells/well, or µ-clear imaging plates. For RNAscope, cells were plated into multiwell chamber slides with a removable chamber (IBIDI or ThermoFisher Scientific, 177445PK). Cells were exposed to ZIKV (MOI:1 for all GBM or HDB cells or MOI:3 for primary GBM cells; MOI 10 for ZIKV-mCh, all cell types) for 2 h at 37 °C, washed with PBS and maintained for 48 or 72 h. Cells for MOCK infection were seeded in separate plates and processed in parallel.

Brain tumour tissue slices were maintained in PTFE inserts in 6 well plates. Virus addition was performed by dispensing 200 µL inoculum onto the air-facing surface of the slice, with the remaining 800 µL inoculum into the well under the insert. Total inoculation was  $1 \times 10^7$  PFU of ZIKV, with adsorption period of 4 hours, then inserts were washed with PBS and transferred to a maintenance plate. Media was changed every 48h by transferring PTFE inserts to new equilibrated maintenance plates. After 3 or 7 days, slices were either transferred into RNAlater RNA stabilization Reagent (ThermoFisher, AM7020) for ZIKV RNA quantification by RT-qPCR, or fixed in 4% formaldehyde for 4 hours at RT or overnight at 4 °C for IF or smFISH.

### Conditioned media collection and experiments

Conditioned media was harvested from GBM cell lines, GBM11b- and GBM11b+ cells cultured in 200,000 cells per ml of media, 48 hours post plating, to generate LineCM, 11b-CM and 11b+CM conditioned media stocks respectively. Where indicated, cells/media were also supplemented with 10 µg/ml poly(I:C) (InvivoGen, tlr1-pic) during conditioning, also for 48 hours total, to generate Pi:c-LineCM, Pi:c-11b-CM and Pi:c-11b+CM conditioned media stocks respectively. 0.22 µm syringe filters were used to remove cell and debris contamination at the time of harvesting. Media was frozen in aliquots at -80 °C if not used immediately.

For RT-qPCR analysis of ZIKV infection following CM treatment ([Figure 6B](#)), cells were incubated in CM without poly(I:C) diluted 50:50 with NSC media for 12h before infection, and for 48h after infection.

For conditioned media RNA-Seq experiments ([Figures 6C, S5E, and S5F](#)), GBM E22 or GBM E34 cells were plated in a 24 well plate and incubated in 150 µL CM + 250 µL NSC media for 48 h. Individual RNA-Seq libraries were prepared using 11b+CM from 3 separate patient GBM11b+ fractions and 3 LineCM controls.

### IFNβ and ruxolitinib experiments

For the IFNβ dose response on ZIKV infection (RT-qPCR analysis), GBM lines were incubated in NSC media supplemented with appropriate doses of IFNβ (R&D Systems, 8499-IF-010) 24 h before ZIKV infection and after viral adsorption until RNA harvesting 48 h after infection.

For the assessment of JAK/STAT signalling by Western, GBM lines in 6 or 12 well plates were incubated in NSC media or CM media supplemented with appropriate doses of IFNβ or ruxolitinib (Selleck Chemicals, S1378) for 3 h. Then the cells were washed 1x in cold DPBS and harvested in 1x sample buffer with protease and phosphatase inhibitors (Fisher Scientific, 78441).

For ruxolitinib and IFNβ rescue experiments in GBM E22 cells, base media or CM were supplemented with ruxolitinib at the indicated concentrations. Cells were pre-treated with CM or base media +/- recombinant IFNβ, +/- ruxolitinib, for 24 h prior to ZIKV infection, then grown in unsupplemented base media for 48 h prior to fixation/lysis for assay of productive infection.

For IFN $\beta$  treatment combined with ZKV infection in HDB slice culture, 3 slices were left uninfected (MOCK), 3 were infected with ZIKV as detailed above, and 3 were pretreated with 100 pg/mL IFN $\beta$  for 24 h before ZIKV infection. Slices were fixed at 72 h.p.i. and processed for IF.

### Western blotting

0.3-2 million cells were pelleted, washed once in cold PBS, spun down, the cell pellet aspirated dry and frozen on dry ice. Proteins were extracted in RIPA buffer and protein concentration quantified using a BCA assay or a Direct Detect Spectrometer.

For the STAT-1 Westerns, cells growing in 12 or 6 well plates were washed in cold PBS, then sample buffer added directly to the cells at a ratio of  $5 \times 10^6$  cells/ml sample buffer. The cells were then scraped off the plate, transferred straight to tubes on ice, and frozen at -80 °C until use. The lysate was thawed on ice, heated for 5 min at 95 °C and, vortexed briefly, spun at 14000rpm for 8 min at 4 °C and the supernatant collected. For western blots, extracts were separated by SDS-PAGE on 4-12% Bis-Tris NuPage gels (Invitrogen) and blotted onto nitrocellulose membrane before blocking for 1 h with Intercept (TBS) blocking buffer (LI-COR). All antibodies (**Table S5**) were diluted in 50:50 Intercept blocking buffer: TBS-tween (TBST 0.1%). Primary antibodies were incubated on the blots overnight at 4 °C. Blots were washed in TBST, then fluorescent conjugated antibodies (LI-COR, 1:5000) added at room temperature for 2 h. Finally, blots were washed in TBST and imaged using the LI-COR Odyssey system.

### Immunofluorescence (IF) for dissociated adherent cells

Cells were fixed using 4% paraformaldehyde (PFA) for 10 min, then washed thoroughly with PBS. Cells were permeabilized with PBS containing 0.5% Triton-X-100 for 5 min, then blocking solution added (PBS with 0.5% bovine serum albumin (BSA), 0.1% Triton X-100) for at least 1 hour but up to 2 days. All antibodies are listed in **Table S5**. Primary antibodies were added in blocking solution for 2 h at 37 °C, or overnight at 4 °C. Cells were then washed three times for 10min with PBST (PBS with 0.1% Triton X-100). Cells were stained with an appropriate secondary antibody (Alexa Fluor 488, 594 or 647; 1:500, Invitrogen) for 1 h at room temperature. Cells were washed twice for 5 min with PBST, once with PBS, incubated in DAPI for 10 min (1:5,000 in PBS), then washed with PBS and imaged either in the plate on a Leica SP5 confocal at 20x or 40x or Operetta CLS at 20x.

### Immunofluorescence for GBM and HDB slices

After fixation slices or T0 tissue were washed 3 times >10 min in PBS. Samples were placed in 20% sucrose for cryoprotection for 24–48 h at 4 °C, then embedded in optimal cutting temperature (OCT) compound, frozen in an ethanol/dry ice bath and stored at -80 °C. 14-16  $\mu$ m cryosections were cut onto superfrost slides using a CM3050S cryostat (Leica Microsystems) and stored at -80 °C until IF staining or smFISH. For IF, slides were allowed to equilibrate at RT in PBS for 15 min, then permeabilised with PBS containing 1% Triton-X-100 for 15 min. Blocking solution was then added for 1 h, and the slides incubated in primary antibodies in blocking solution overnight at 4 °C. Sections were then washed four times for 15 min with PBST, and appropriate secondary antibodies added (Alexa Fluor 488, 594 or 647; 1:500, Invitrogen) in blocking solution for 1.5-2 h at room temperature. Cells were washed twice for 15 min with PBST, once with PBS, incubated in DAPI for 10 min, then washed with PBS and coverslips applied using Prolong Gold or Diamond.

### smFISH (RNAscope) sample preparation

HDB or GBM tissue sections were stored at -80 °C and transferred directly to ice-cold 4% paraformaldehyde (PFA) solution for 45 min. Slides then underwent citrate buffer (1x, pH 6.0, Sigma-Aldrich, C9999) heat-induced antigen retrieval at 95 °C for 15 min. Slides were then washed and dehydrated in PBS (1X) and ethanol gradients from 50% to 100% for a total of 30 min. Slides were air-dried before automated single molecule fluorescent *in situ* hybridization (smFISH) protocol. Cell cultures adherent to plastic or positively charged glass slides were fixed in 4% PFA for 45 min, dehydrated in ethanol gradients and stored at -20 °C in 100% ethanol for ~ 2 weeks. Slides were rehydrated in ethanol gradients from 100% to 50% directly before the automated smFISH protocol.

Multiplex smFISH was performed on a Leica BondRX fully automated stainer, using RNAscope® Multiplex Fluorescent V2 technology (Advanced Cell Diagnostics, 322000). GBM tissue section slides underwent heat-induced epitope retrieval (HIER) with Epitope Retrieval Solution 2 (pH 9.0, Leica AR9640) at 95 °C for 10 min. HDB tissue sections underwent the above HIER for 5 min, and adherent cells did not undergo heat treatment. GBM, HDB tissue and cells were then incubated in RNAscope® Protease III reagent (ACD 322340) at 42 °C for 15, 10 and 5 min, respectively. All slides were then treated with RNAscope® Hydrogen Peroxide (ACD 322330) for 10 min at RT to inactivate endogenous peroxidases.

All double-Z mRNA probes were designed against human genes by ACD for RNAscope® on Leica Automated Systems and are listed in **Table S6**. Further information is readily available from the manufacturer (<https://acdbio.com/catalog-probes>).

Slides were incubated in RNAscope 2.5 LS probes for 2 h at RT. DNA amplification trees were built through consecutive incubations in AMP1 (preamplifier, ACD 323101), AMP2 (background reduction, ACD 323102) and AMP3 (amplifier, ACD 323103) reagents for 15 to 30 min each at 42 °C. Slides were washed in LS Rinse buffer (ACD 320058) between incubations.

After amplification, probe channels were detected sequentially via HRP-TSA labelling. To develop the C1-C3 probe signals, samples were incubated in channel-specific horseradish peroxidase (HRP) reagents for 30 min, TSA fluorophores for 30 min and HRP-blocking reagent for 15 min at 42 °C. The probes in C1, C2 and C3 channels were labelled using Opal520 (Akoya FP1487001KT),

Opal570 (Akoya FP1488001KT), and Opal 650 (Akoya FP1496001KT) fluorophores (diluted 1:500). The C4 probe complexes were first incubated with TSA–Biotin (Akoya NEL700A001KT, 1:250) for 30 min at RT, followed by streptavidin-conjugated Atto425 (Sigma 56759, 1:400) for 30 min at RT. Samples were then incubated in DAPI (Sigma, 0.25 µg /ml) for 20 min at RT, to mark cell nuclei. Slides were briefly air-dried and manually mounted using ~90 µl of Prolong Diamond Antifade (Fisher Scientific) and standard coverslips (24 × 50 mm<sup>2</sup>; Fisher Scientific). Slides were dried at RT for 24 h before storage at 4 °C for >24 h before imaging.

### smFISH and IF automated imaging and analysis

#### *Slice culture imaging and analysis*

Slides and plates were imaged on either a Leica SP5 confocal or an Operetta high-content imaging system (Perkin-Elmer) with Harmony software, settings as detailed in Table S7. Image analysis was carried out using Fiji, Python, or Harmony 4.9 software (Perkin Elmer). Data and statistical analyses were carried out in Excel or GraphPad Prism. Brightness and contrast were adjusted for display, always to the same levels when comparing across tissues.

To locate whole-tissue sections or regions of interest for high-resolution imaging, entire slides were initially scanned under low magnification using a ×5 numerical aperture (NA) 0.16 objective (pixel size: 7.2 µm). Regions of interest for ×40 scans were manually selected on low-magnification previews. Selected ×40 fields were imaged with an 8% overlap. The high-resolution smFISH images of cells and tissue sections were acquired on the spinning-disk confocal mode using a sCMOS camera and a ×40 NA 1.1 automated water-dispensing objective. Each field was imaged as a z-stack consisting of 20 planes, with a 1 µm incremental step size.

To segment single nuclei, myeloid cells, progenitors and ZIKV+ cells, analysis scripts were created in Harmony 4.9 using customisable building block functionality. To identify single nuclei, Gaussian blurred DAPI images were segmented using intensity, size, and contrast thresholds. To identify RUNX1+/CD68+ myeloid cells and SOX2+ progenitor cells, a peri-nuclear region was created by increasing the area of each nucleus by 3 µm<sup>2</sup>. RUNX1, CD74 and SOX2 mRNA puncta were then quantified within the nucleus (+3 µm<sup>2</sup>) and cell populations were selected based on spot number, intensity, size, and contrast thresholds. To analyse ZIKV in HDB tissue sections, ZIKV+ cells were identified by segmenting the cytoplasm around the nuclei based on ZIKV signal intensity thresholding. To analyse ZIKV in GBM tissue and cell cultures, ZIKV+ regions were segmented based on ZIKV signal intensity thresholding and morphology characteristics. ZIKV+ nuclei were then segmented within these regions based on Gaussian smoothed DAPI intensity characteristics. Cell populations were quantified as a ratio of total nuclei analysed.

To identify IBA1 and SOX2+ cells in T0 sections, the background and autofluorescence of the tissue was corrected by subtracting the image of an empty channel. SOX2+ cells were then selected based on SOX2 signal intensity thresholding. IBA1 + image regions were identified in the tissue, and IBA1+ cells were identified based on both nuclear overlap of at least 30% with these regions and IBA1 nuclear signal intensity thresholding.

To identify SOX2 and ZIKV positive cells after IF staining in HDB tissue, nuclei and cell cytoplasm were segmented in Harmony. SOX2+ cells were selected based on nuclear SOX2 signal intensity thresholding and ZIKV+ cells selected based on ZIKV intensity thresholding in the whole cell. Double SOX2+ and ZIKV+ cells were counted and expressed as a percentage of the SOX2+ cells. 4-30 thousand SOX2+ cells were analysed per condition, across 3 slices per condition, 1-3 replicate cryosections per slice, in 1 HDB sample.

#### *Dissociated adherent cell imaging and analysis*

For counting SOX2 or IBA1 positive cells representative fields of mock infected cultures were imaged at 20 or 40x on the confocal, then image processing and nuclei counting was implemented with a python script using the scikit-image library. First, background and flatfield correction was applied to the input image (I) based on Gaussian ( $\sigma=5$ ) blurred input image (GI). The corrected image was then calculated using the equation:  $I/(GI/\max(GI)) - 0.3*GI$ . Afterwards, multiotsu thresholding and watershed algorithm was employed to segment the nuclei on different channels (both DAPI and SOX2). Among the segmented regions, SOX2 positive nuclei were then picked out if the overlapping area of the regions from two channels was greater than 80% of that in the DAPI channel.

IBA1 positive cells were either counted manually or by nuclear signal intensity thresholding.

For counting SOX2 and IBA1 positive cells imaged on the Operetta CLS, Harmony 4.9 software was used. To identify single nuclei, Gaussian blurred DAPI images were segmented using intensity, size, and contrast thresholds. SOX2 or IBA1 cell populations were selected based on nuclear intensity thresholds.

To calculate the average proportion of SOX2 and IBA1 positive cells in the GBM, GBM11b- and GBM11b+ fractions, cell counts were performed from at least 3 separate GBM samples for each fraction.

### Zika viral RNA quantification

RNA was extracted from cells using the RNeasy® Mini Kit (Qiagen) with DNase treatment. Brain slices stored in RNAlater were disrupted and homogenised using the TissueRuptor® II (Qiagen) and RNA extracted with the RNeasy® Lipid Tissue mini Kit (Qiagen) following the manufacturer's protocol. Total RNA was then quantified by NanoDrop 8000 quantification (Thermo Fisher Scientific). RT-qPCR was carried out using TaqMan® chemistry, with a commercial quantification kit (Genesig Standard Zika Virus Quantification Kit, PrimerDesign), using One-Step 2X RT-qPCR Reagent (PrimerDesign).

**RNA extraction, library preparation and sequencing**

For all samples, RNA was extracted using Qiagen RNeasy Micro Plus kit and analysed on Bioanalyser to confirm RIN >8. Library preparation was undertaken using NEB Ultra II Directional Kit (Poly A enrichment). For primary cell ZIKV-mCh sorted fractions with smaller cell numbers and lower input RNA concentrations, Takara Smartseq pico V2 library preparation (Ribosomal depletion) was used. In each case library preparation was performed according to manufacturers' instructions. Paired end sequencing was performed using Illumina Novaseq PE50.

**Bulk RNA-Seq Analysis**

Quality checks on the raw fastq files were performed using FastQC (v0.11.8) (Andrews, 2010), summarised with MultiQC (v1.9) (Ewels et al., 2016). The fastq files were subsampled (to 50M reads and 25M reads for the mCherry and myeloid cell experiment respectively) to achieve a uniform sequencing depth (Mohorianu et al., 2017). For the mCherry experiment, the first 3 nucleotides for both forward and reverse reads were trimmed using TrimGalore (v0.6.4\_dev, based on cutadapt v3.4) (Kruger, 2012) to account for low sequence quality. The resulting fastq files were aligned to the *H. sapiens* reference genome (build GRCh38.p13) using STAR (v2.7.0a) with default parameters (Dobin et al., 2013) The count matrices were generated using featureCounts (subread package, v2.0.0) (Liao et al., 2014).

Further quality checks on the count matrices included density and violin plots, illustrating the abundance distributions across samples, MA plots for pairwise comparisons of replicates focusing on the per-gene fold-differences across abundances. In addition, Jaccard Similarity Index (JSI) heatmaps show the robustness of the most highly expressed genes across samples, dendograms exemplify the hierarchical similarity in transcriptomic signatures and Principal Component Analysis (PCA) plots present the inter-sample relationships under a dimensionality reduction, to assess similarity.

A noise analysis was performed using noisyR (v1.0.0) (Moutsopoulos et al., 2021) to correct for artificially high fold-changes exhibited by low expression genes. The noise threshold, added to each expression matrix, was calculated to be 300 for the mCherry experiment and 15 for the myeloid cell experiment, with ~19k and ~23k genes kept for further analysis respectively. A quantile normalisation (Bolstad et al., 2003) was then applied on the denoised matrices.

Differential expression (DE) analysis was performed using both edgeR (v3.34.0) (McCarthy et al., 2012) and DESeq2 (v1.32.0) (Love et al., 2014). The comparisons focused on GBM\_HR vs GBM\_MR and Zika positive vs negative for the mCherry experiment, and control vs myeloid cell media type for the myeloid cell experiment. Due to the similarity of the two conditions for individual cell types in the myeloid cell experiment, DE was performed both on each cell type individually (GBM E22, GBM E34, HDB) and on the whole dataset.

An enrichment analysis was performed on all DE genes in each comparison (for robustness the intersection between edgeR and DESeq2 was considered; the two packages largely agreed after the noise correction (Moutsopoulos et al., 2021), with all genes expressed in each dataset (with maximum expression higher than the noise threshold) as background using the g:profiler (<https://biit.cs.ut.ee/gprofiler/gost>) R package (v0.2.0) (Raudvere et al., 2019) and Reactome datasets (Viteri et al., 2019).

For the ZIKV-mCh experiment, the genes potentially regulated by ZIKV were identified by splitting the viral genome into 30 nucleotide windows (with 20nt overlap) and aligning them to the *H. sapiens* reference genome (build GRCh38.p13) using STAR (v2.7.0a) with default parameters (Dobin et al., 2013) The genes proximal to the aligned coordinates were then identified.

**CIBERSORT Analysis**

The bulk RNA-Seq libraries were submitted to the CIBERSORT analysis pipeline (Newman et al., 2015) in absolute mode using the LM22 gene signature file, permutations = 500, quantile normalisation disabled. The 22 gene types incorporated in this scheme were collapsed for display purposes to the 9 gene types displayed by summation of the absolute scores for relevant subtypes. For example, plotted 'B-cells' score represents the sum of absolute scores for B-cell naïve, B-cell memory and Plasma cell LM22 categories. Likewise 'T-cells', 'NK cells', 'myeloid cell', 'Dendritic cells', 'Mast cells' are each composite terms representing the sum of the relevant subtype scores.

**Single cell RNA-Seq analysis****Plate-based scRNA-seq (ZIKV mCh+ libraries)**

Plate based scRNA-seq was performed with the NEBNext Single Cell/Low Input RNA Library Prep Kit for Illumina (New England Biolabs Inc, E6420L). Briefly, single cells were sorted into a pre-prepared 384-well plate (Eppendorf, Cat. No. 0030128508) or 96-well plate (Eppendorf, Cat. No. 0030128648) containing 2 µl of 1X NEBNext Cell Lysis Buffer. Sorted single cells were sealed and spun at 100 x g for 1 minute then immediately frozen on dry ice and stored at -80 °C.

cDNA generation was then performed in an automated manner on the Agilent Bravo NGS workstation (Agilent Technologies). Briefly, 1.6 µl of Single Cell RT Primer Mix was added to each well and annealed on a PCR machine (MJ Research Peltier Thermal Cycler) at 70°C for 5 minutes. 4.4 µl of Reverse Transcription (RT) mix was added to the mixture and further incubated at 42°C for 90 minutes followed by 70°C for 10 minutes to generate cDNA. 22 µl of cDNA amplification mix containing NEBNext Single Cell cDNA PCR MasterMix and PCR primer was mixed with the cDNA, sealed and spun at 100 x g for 1 minute. cDNA amplification was then performed on a PCR machine (MJ Research Peltier Thermal Cycler) with 98°C 45 s, 20-25 cycles of [98°C 10 s, 62°C 15 s, 72°C 3 mins], 72°C 5 mins.

The plate containing the amplified cDNA was purified with an AMPure XP workflow (Beckman Coulter, Cat No. A63880) and quantified with the AccuClear Ultra High Sensitivity dsDNA kit (Biotium, Cat. No. 31028). ~10 ng of cDNA was stamped into a fresh plate for sequencing library preparation.

Sequencing libraries were then generated on the Agilent Bravo NGS workstation (Agilent Technologies). Purified cDNA was fragmented by the addition of 0.8  $\mu$ l of NEBNext Ultra II FS Enzyme Mix and 2.8  $\mu$ l of NEBNext Ultra II FS Reaction buffer to each well and incubated on a PCR machine (MJ Research Peltier Thermal Cycler) 72°C 15 mins, 65°C 30 mins. A ligation mixture was then prepared containing NEBNext Ultra II Ligation Master Mix, NEBNext Ligation Enhancer and 100  $\mu$ M Illumina compatible adapters (Integrated DNA Technologies) and 13.4  $\mu$ l added to each well of the plate. The ligation reaction was incubated on the Agilent workstation at 20°C for 15 minutes and then purified and size selected with an AMPure XP workflow (Beckman Coulter, Cat No. A63880).

20  $\mu$ l of KAPA HiFi HS Ready Mix (Kapa Biosystems, Cat. No. 07958927001) was then added to a pre-prepared plate (Eppendorf, Cat. No. 0030128508) containing 100  $\mu$ M i5 and i7 indexing primer mix (50  $\mu$ M each) (Integrated DNA Technologies). The indexing primers pairs were unique to allow multiplexing of up to 384 single cells in one sequencing pool. The plate containing the PCR Master Mix and indexing primers was stamped onto the adapter ligated purified cDNA, sealed and spun at 100 x g for 1 minute. Amplification was performed on a PCR machine (MJ Research Peltier Thermal Cycler) with 95°C 5 min, 8 cycles of [98°C 30 s, 65°C 30 s, 72°C 1 min], 72°C 5 mins. The PCR products were pooled in equal volume on the Microlab STAR automated liquid handler (Hamilton Robotics) and the pool purified and size selected with an AMPure XP workflow (Beckman Coulter, Cat No. A63880). The purified pool was quantified on an Agilent Bioanalyser (Agilent Technologies) and sequenced on one lane of an Illumina HiSeq 4000 instrument (75bp paired end, HiSeq 4000 150 cycle kit).

### Preprocessing

10X v2 single-nucleus RNAseq data was aligned to human genome version GRCh38 using the cellranger software and processed with the CellBender ([Fleming et al., 2019](#)) algorithm before any further downstream analysis to remove ambient RNA. SmartSeq data was aligned to human genome version GRCh38 augmented for the ZIKV genome with the STAR algorithm ([Dobin et al., 2013](#)). We further used the scrublet algorithm ([Wolock et al., 2019](#)) to remove doublets, manually choosing doublet score thresholds for each sample, based on the bimodal histograms of doublet scores.

### Quality control

We plotted QC plots using number of detected genes, number of counts and percent of counts coming from mitochondrial genes and removed outlier cells. For the SmartSeq data removed cells had less than 2500 detected genes, more than 12000 detected genes, less than two million reads or more than 10% of reads coming from mitochondrial genes. For the 10X data removed cells had less than 500 detected genes, more than 5000 detected genes, less than 400000 counts or more than 10% of counts for mitochondrial genes.

### Calculation of glioma cells subtype scores

We then calculated glioma cell subtype score according to methods previously outlined ([Neftel et al., 2019](#)) Briefly, for genes i and sample j, this meant considering only genes with  $E_a > 4$ , where  $E_a$  is given by  $E_a(i) = \log_2(\text{average}(TPM_{i,1\dots n}) + 1)$ . Furthermore, expression levels were defined as  $E_{i,j} = \log_2(TPM_{i,j}/10+1)$ , based on which relative expression levels were defined as  $Er_{i,j} = E_{i,j} - \text{average}[E_{i,1\dots n}]$ . These relative expression levels, were then used to calculate gene signature scores, as  $SC_j(i) = \text{average}[Er(G_j,i)] - \text{average}[Er(G_j^{\text{cont}},i)]$ , where  $Er(G_j,i)$  is the average relative expression of genes included in the expression signature of interest (mesenchymal cell-like, oligodendrocyte precursor cell-like, astrocyte-like, neural progenitor cell-like), obtained from Extended Data Table 2 in the original publication ([Neftel et al., 2019](#)) and  $Er(G_j^{\text{cont}},i)$  is a control gene set. This control gene set was defined as in the original publication, by binning all genes into 30 groups based on their expression and then selecting for each gene in the gene signature score 100 control genes of similar aggregate expression.

### Normalisation and clustering

We used the scanpy python package ([Wolf et al., 2018](#)) to normalise and log-transform the data, as well as regress out the effects of total counts and mitochondrial counts. We then used the BBKNN algorithm ([Polański et al., 2019](#)) for batch alignment followed by Louvain clustering.

### Classification of primary cell types

We visualised the expression of brain cell type markers, as well as glioma cell subtype scores for each cluster in a heatmap. Based on this we classified a cell as non-malignant if it displayed distinct expression of typical markers of a brain cell type (e.g., myeloid cell, astrocytes, excitatory neuron) and had low glioma cell subtype scores. Similarly, we classified a cell as glioma cell if it had a high expression of glioma cell subtype scores and expressed indistinct expression of multiple cell type markers.

### Classification of glioma cell subtypes

We recalculated the glioma cell subtype scores only on the subset of glioma cells, so we excluded non-malignant cells, such as myeloid cells, astrocytes and neurons. We then classified each glioma cell into the subtype for which it had the highest score.

### Classification of myeloid cell states

We used the CCA algorithm ([Stuart et al., 2019](#)) to classify our myeloid cell data into states defined in a previous scRNAseq study ([Sankowski et al., 2019](#)), using the 2000 most variable genes in the reference data set.

### RT-qPCR

Taqman RT-qPCR (Thermo Fisher) inventoried human assays were used according to manufacturers' instructions, probe IDs available on request.

**QUANTIFICATION AND STATISTICAL ANALYSIS**

All statistical comparisons were undertaken using Graphpad Prism software v9.0.0. Summary statistics and specifics of statistical tests and their results are detailed in the figure legends. In the context of primary human samples, n refers to biological replicates corresponding to distinct primary patient/donor samples unless otherwise stated.